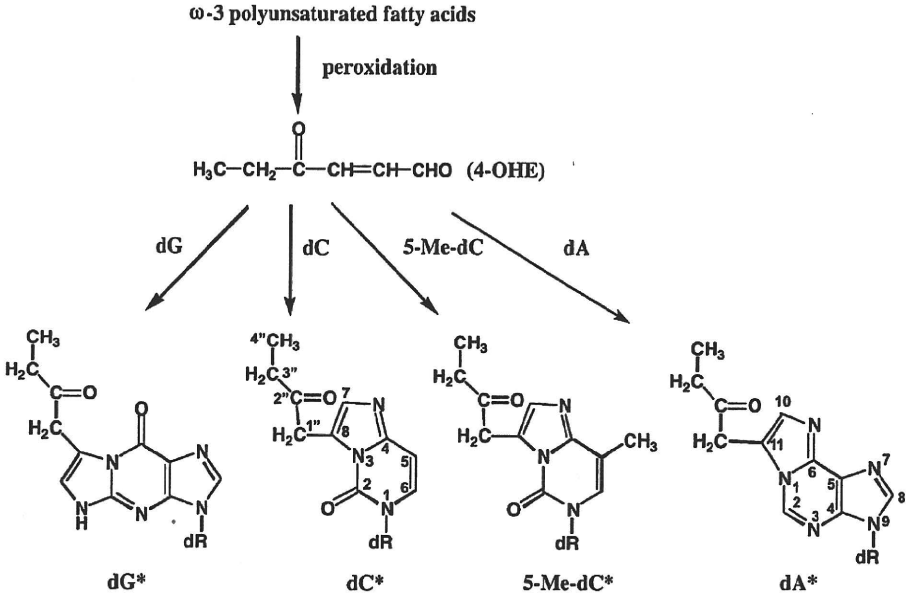


**Figure 1.** Structures of 4-OHE–DNA adducts.

Samples were resuspended in 50 μL of Milli-Q water before LC/ESI-MS/MS analysis.

**LC/ESI-MS/MS Analyses.** The LC/MS/MS analysis was performed using a Quattro Ultima Pt triple stage quadrupole mass spectrometer (Waters-Micromass, United States) equipped with a Shimadzu LC system (Shimadzu, Japan). An aliquot of each sample (40 μL) was injected and separated by a Shim-pack XR-ODS column (3.0 mm × 75 mm, Shimadzu, Japan). The column was eluted with a linear gradient of 15–80% methanol in water from 0 to 15 min at a flow rate of 0.2 mL/min and then was switched back to the initial condition of 15% methanol in water from 15 to 27 min. Mass spectral analysis was performed in the positive ion mode, using nitrogen as the nebulizing gas. Experimental conditions were set as follows: ion source temperature, 130 °C; desolvation temperature, 380 °C; cone voltage, 35 V; desolvation gas flow rate, 700 L/h; and cone gas flow rate, 35 L/h. Argon was used as the collision gas. The collision energy and characteristic reactions (base ion→product ion) monitored for the different DNA adducts are as follows: dC* (10 eV, 321.8→205.8), [$^{15}N_3$]-dC* (10 eV, 324.8→208.6), 5-Me-dC* (20 eV, 335.9→220.0), dA* (10 eV, 345.8→229.8), [$^{15}N_5$]-dA* (10 eV, 351.0→234.8), and dG* (20 eV, 362.0→245.9).

The amount of each DNA adduct was quantified by calculating the peak area ratio of the target DNA adduct and its specific internal standard ([$^{15}N_3$]-dC* was used for dC* and 5-Me-dC*, and [$^{15}N_5$]-dA* was used for dA* and dG*). Calibration curves were obtained using authentic standards spiked with isotopically labeled internal standards. The concentration of 2′-deoxyguanosine (dG) in each DNA sample was also monitored by the SPD-10Avp UV–visible detector in the Shimadzu LC system, and the adduct levels in each sample were calculated using the amount of dG. The number of DNA adducts per $10^9$ bases was calculated by the following equation: number of DNA adducts per $10^9$ bases = adduct level (fmol/μmol dG) × 0.218(μmol dG/μmol dN), as described previously (*21*).

The signal-to-noise ratio (S/N: peak to peak) of the adduct peak was calculated by using the Masslynx V4.0 software. The detection limits of the adducts, for which the peaks were expected to have an S/N of 3, were 0.13 (dG*), 0.35 (dA*), 0.41 (Me-dC*), and 0.08 fmol (dC*). This sensitivity was sufficient to detect 0.5–2.7 adducts per $10^9$ bases when using 50 μg of DNA. The quantification limits of the peaks that were expected to have an S/N of 10 were also estimated to be 0.26 (dG*), 0.92 (dA*), 0.87 (Me-dC*), and 0.23 fmol (dC*).

**Table 1. NMR Data of dC* in DMSO-$d_6$[a]**

| position | $\delta_C$ (ppm) | $\delta_H$ (ppm) | multiplicity, *J* (Hz) |
|---|---|---|---|
| 2 | 146.8 | | |
| 4 | 145.1 | | |
| 5 | 98.9 | 6.62 | d, 8.1 |
| 6 | 127.8 | 7.61 | d, 8.1 |
| 7 | 132.6 | 7.11 | s |
| 8 | 123.0 | | |
| 1′ | 84.7 | 6.30 | t, 6.8 |
| 2′ | 40.0 | 2.14 | m |
| 3′ | 70.4 | 4.26 | m |
| 3′-OH | | 5.26 | br |
| 4′ | 87.6 | 3.81 | q, 3.7 |
| 5′ | 61.2 | 3.56 | dd, 3.7, 12.2 |
| | | 3.60 | dd, 3.7, 12.2 |
| 5′-OH | | 5.13 | br |
| 1″ | 38.7 | 4.11 | d, 17.7 |
| | | 4.15 | d, 17.7 |
| 2″ | 206.7 | | |
| 3″ | 34.5 | 2.54 | q, 7.3 |
| 4″ | 7.6 | 0.95 | t, 7.3 |

[a] Chemical shifts in ppm from TMS as an internal standard.

## Results

**Structure Confirmation of 4-OHE Adducts with dC, 5-Me-dC, and dA.** 4-OHE reacts not only with dG but also with dC, 5-Me-dC, and dA to yield adducts (dC*, 5-Me-dC*, and dA*). The structures of dC*, 5-Me-dC*, and dA* were determined as shown in Figure 1, mainly by the MS, NMR, and X-ray crystallography data. $^1H$ and $^{13}C$ NMR data for these synthetic compounds are provided in Tables 1–3.

The molecular formula of dC* is consistent with $C_{15}H_{19}N_3O_5$, as determined by high-resolution electrospray ionization mass spectrometry (HRESI-MS) [positive ion mode, *m/z* 344.1192 $(M + Na)^+$ 344.1222 calcd for $C_{15}H_{19}N_3O_5Na$]. The HRESI-MS/MS spectrum of *m/z* 322.1 revealed product ions at *m/z* 206.0923 (Δ −0.11 mDa as $C_{10}H_{12}N_3O_2$: base + $H_2$), *m/z* 150.0659 (Δ −0.31 mDa $C_7H_8N_3O$: base + $H_2$ − $C_2H_5CO$), and *m/z* 121.0631 and *m/z* 57.0332 (Δ −0.25 mDa $C_3H_5O$: etheno ring side chain). The UV $\lambda_{max}$ in $H_2O$ was 277 nm (ε 11460). The $^1H$ and $^{13}C$ NMR spectra showed additional characteristic signals: $CH_2$ ($\delta_H$ 4.11 and 4.15, $\delta_C$ 38.7), C=O ($\delta_C$ 206.7), $CH_2$ ($\delta_H$ 2.54, $\delta_C$ 34.5), and $CH_3$ ($\delta_H$ 0.95, $\delta_C$ 7.6), as compared with those of dC (Table 1). dC* generated a highly

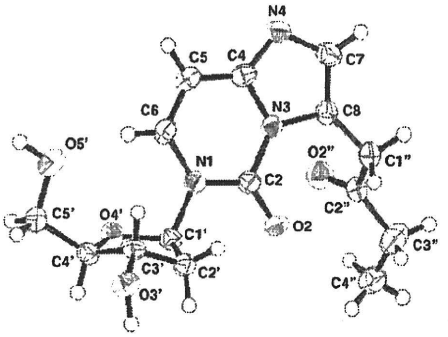


**Figure 2.** Crystal structure of dC*.

**Table 2. NMR Data of 5-Me-dC* in DMSO-$d_6$[a]**

| position | $\delta_C$ (ppm) | $\delta_H$ (ppm) | multiplicity, *J* (Hz) |
|---|---|---|---|
| 2 | 146.7 | | |
| 4 | 146.0 | | |
| 5 | 107.2 | | |
| 5-$CH_3$ | 12.8 | 2.14 | brd, 1.0 |
| 6 | 124.2 | 7.42 | brq, 1.0 |
| 7 | 132.4 | 7.11 | s |
| 8 | 123.5 | | |
| 1′ | 84.4 | 6.30 | t, 6.8 |
| 2′ | 39.8 | 2.12 | m |
| 3′ | 70.4 | 4.26 | m |
| 3′-OH | | 5.26 | d, 4.3 |
| 4′ | 87.5 | 3.79 | dd, 3.7 |
| 5′ | 61.3 | 3.56 | dt, 4.3, 12.1 |
| | | 3.62 | ddd, 3.7, 5.0, 12.1 |
| 5′-OH | | 5.06 | t, 5.2 |
| 1″ | 38.7 | 4.10 | d, 17.7 |
| | | 4.15 | d, 17.7 |
| 2″ | 206.7 | | |
| 3″ | 34.5 | 2.53 | q, 7.3 |
| 4″ | 7.6 | 0.95 | t, 7.3 |

[a] Chemical shifts in ppm from TMS as an internal standard.

crystalline product, and thus, further structure elucidation was performed by X-ray crystallography. The compound was recrystallized by an ethanol:water (1:1) solvent system and yielded colorless prisms. An Oak Ridge Thermal Ellipsoid Program (ORTEP) drawing of dC* is shown in Figure 2. The sugar of dC* adopts the C(3′)-endo conformation, and the glycosidic torsion is in the anti form.

The molecular formula of 5-Me-dC* is consistent with $C_{16}H_{21}N_3O_5Na$, as determined by HRESI-MS [positive ion mode, *m/z* 358.1372, $(M + Na)^+$ 358.1379 calcd for $C_{15}H_{19}N_3O_5Na$]. The HRESI-MS/MS spectrum of *m/z* 336.2 revealed product ions at *m/z* 220.1079 (Δ −0.15 mDa as $C_{11}H_{14}N_3O_2$: base + $H_2$), *m/z* 164.0816 (Δ −0.26 mDa as $C_8H_{10}N_3O$: base + $H_2$ − $C_2H_5CO$), and *m/z* 135.0788, *m/z* 108.0679, and *m/z* 57.0333 (Δ −0.23 mDa as $C_3H_5O$: etheno ring side chain). The UV $\lambda_{max}$ in $H_2O$ was 278 nm (ε 11930). The $^1H$ and $^{13}C$ NMR spectra showed almost the same additional characteristic signals of dC*: $CH_2$ ($\delta_H$ 4.10 and 4.15, $\delta_C$ 38.7), C=O ($\delta_C$ 206.7), $CH_2$ ($\delta_H$ 2.53, $\delta_C$ 34.5), and $CH_3$ ($\delta_H$ 0.95, $\delta_C$ 7.6), as compared with those of 5-Me-dC (Table 2). Further structure determination was accomplished by various two-dimensional NMR techniques, such as correlation spectroscopy (COSY), heteronuclear multiple quantum correlation (HMQC), and heteronuclear multiple bond correlation (HMBC), as summarized in Figure 3. The 2-oxo-butyl side chain was attached to C-8 of the imidazole ring, as confirmed by $^1H-^{15}N$ HMBC, where cross-peaks were observed between H-1″ and N-3.

The molecular formula of dA* is consistent with $C_{16}H_{19}N_5O_4$, as determined by HRESI-MS [positive ion mode, *m/z* 368.1320, $(M + Na)^+$ 368.1329 calcd for $C_{16}H_{19}N_5O_4Na$]. The UV $\lambda_{max}$

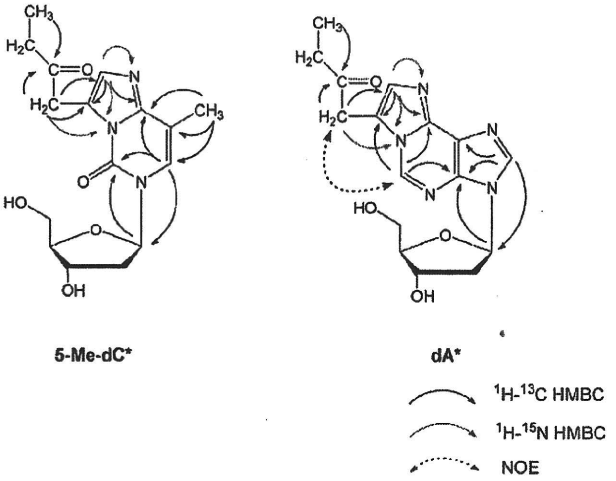


**Figure 3.** Selected 2D NMR results of 5-Me-dC* and dA*.

**Table 3. NMR Data of dA* in DMSO-$d_6$[a]**

| position | $\delta_C$ (ppm) | $\delta_H$ (ppm) | multiplicity, *J* (Hz) |
|---|---|---|---|
| 2 | 135.8 | 8.98 | s |
| 4 | 137.8 | | |
| 5 | 123.1 | | |
| 6 | 140.7 | | |
| 8 | 139.8 | 8.51 | s |
| 10 | 131.8 | 7.34 | s |
| 11 | 118.5 | | |
| 1′ | 84.0 | 6.47 | t, 6.5 |
| 2′ | 39.7 | 2.36 | ddd, 3.4, 6.5, 13.4 |
| | | 2.75 | dt, 6.5, 13.4 |
| 3′ | 70.7 | 4.44 | m |
| 3′-OH | | 5.35 | d, 4.1 |
| 4′ | 88.0 | 3.89 | dt, 3.1, 5.0 |
| 5′ | 61.7 | 3.54 | dt, 5.0, 11.7 |
| | | 3.63 | dt, 5.0, 11.7 |
| 5′-OH | | 4.96 | t, 5.0 |
| 1″ | 36.8 | 4.33 | s |
| 2″ | 206.7 | | |
| 3″ | 34.5 | 2.65 | q, 7.3 |
| 4″ | 7.5 | 0.97 | t, 7.3 |

[a] Chemical shifts in ppm from TMS as an internal standard.

values in $H_2O$ were 232 (ε 25800), 270 (ε 5980), and 279 nm (ε 6080). The HRESI-MS/MS spectrum of *m/z* 346.2 revealed product ions at *m/z* 230.1035 (Δ −0.18 mDa as $C_{11}H_{12}N_5O$: base + $H_2$) and *m/z* 173.0694 (Δ −0.17 mDa as $C_8H_7N_5$: base + $H_2$ − $C_2H_5CO$). The $^1H$ and $^{13}C$ NMR spectra showed additional characteristic signals: $CH_2$ ($\delta_H$ 4.33, $\delta_C$ 36.8), C=O ($\delta_C$ 206.7), $CH_2$ ($\delta_H$ 2.65, $\delta_C$ 34.5), and $CH_3$ ($\delta_H$ 0.97, $\delta_C$ 7.5), as compared with those of dA (Table 3). Further structure determination was accomplished by various two-dimensional NMR techniques, such as COSY, HMQC, HMBC, and nuclear Overhauser effect spectroscopy (NOESY), as summarized in Figure 3. The $^1H-^{13}C$ HMBC spectrum of dA* is shown in Figure 4. The 2-oxo-butyl side chain was attached to C-11 of the imidazole ring, as confirmed by a NOE observed between H-2 and H-1″, and the cross-peaks observed between H-1″ and N-1 by $^1H-^{15}N$ HMBC.

**Reaction of 4-OHE with Calf Thymus DNA in Vitro.** The 4-OHE−DNA adducts formed by the reaction of 4-OHE and calf thymus DNA in vitro were analyzed by HPLC (Figure 5). They were efficiently formed in heat-denatured calf thymus DNA (ss DNA). The yield of the 4-OHE−DNA adducts was about 50 times higher in ss DNA than in ds DNA (data not shown). At a physiological pH, the efficient formation of dC* and 5-Me-dC* was observed (Table 4). This may be due to the higher reactivity of 4-OHE with dC and 5-Me-dC than with dG and dA, rather than steric reasons.

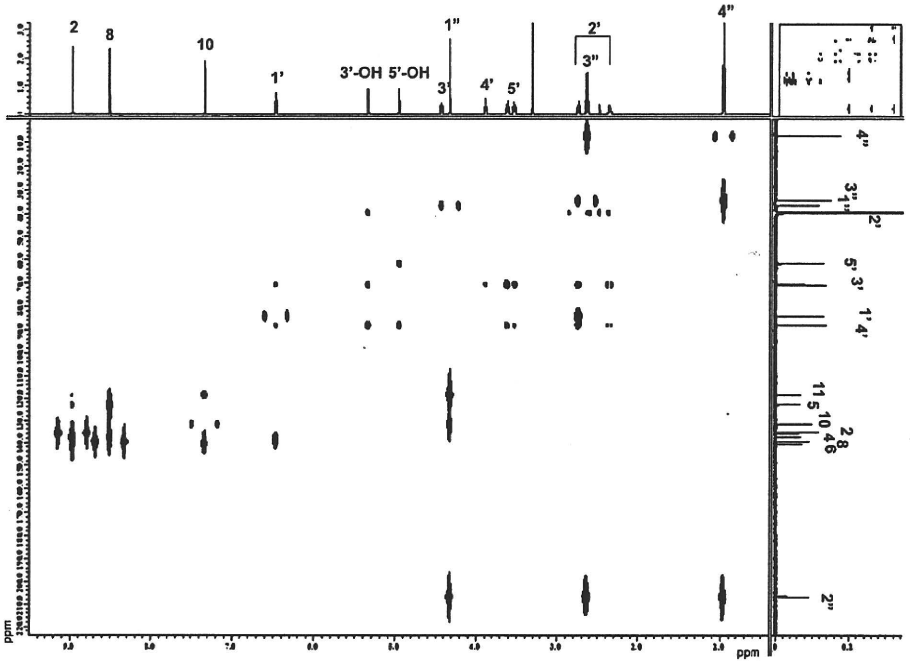


**Figure 4.** $^{1}H-^{13}C$ HMBC spectrum of dA*.

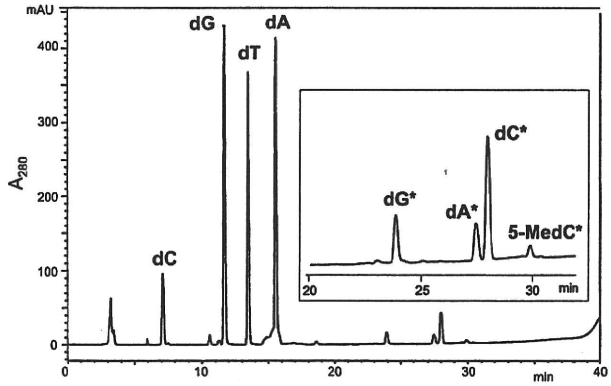


**Figure 5.** Analysis of 4-OHE–DNA adducts formed in vitro by HPLC. Inset, the chromatogram (20–32 min) was expanded. Column: Inertsil ODS-3, 3 $\mu$m, 4.6 mm × 250 mm (GL Sciences Inc., Japan); elution: 0–40 min, linear gradient of acetonitrile (5–30%); elution speed: 0.7 mL/min.

**Table 4. Adduct Levels in 4-OHE-Treated Calf Thymus DNA in Vitro**

| | dC* | dA* | dG* | 5-Me-dC* |
|---|---|---|---|---|
| adduct/$10^3$ each parent base | 41.5/$10^3$ dC | 6.38/$10^3$ dA | 5.58/$10^3$ dG | 61.5/$10^3$ 5-Me-dC |
| $\mu$g adduct/100 $\mu$g DNA | 0.88 | 0.18 | 0.12 | 0.08 |

**LC/MS/MS Analysis of 4-OHE Adducts in Organ DNA from 4-OHE-Treated Mice.** The 4-OHE–DNA adducts in vivo were detected by an LC/MS/MS method. Figure 6 shows typical ion chromatograms of dG*, dA*, 5-Me-dC*, and dC* in DNA isolated from the stomachs of control- and 4-OHE-treated mice. Quantification of the 4-OHE–DNA adducts was achieved using [$^{15}N_5$]-dA* and [$^{15}N_3$]-dC* as internal standards. Some uncertainty remained in the analyses of dG* and 5-Me-dC*, since isotopically labeled dG* and 5-Me-dC* were not used. The results of the DNA adduct formation in mouse stomach and large intestine at 24 h after the oral administration of 4-OHE are summarized in Table 5. Only background levels of the adducts were present in the organ DNA of the vehicle-treated, control mice. In the stomach and large intestine DNA of 4-OHE-treated mice, dC* was detected in the range of 43.71 and 5.57 adducts per $10^8$ bases, respectively. dA* was detected at a comparable level to dC* in these organs. In addition, lower amounts of dG* and 5-Me-dC* were detected in these organ DNAs. The amounts of these DNA adducts were decreased at 72 h after administration (Table 5), and no DNA adduct was detected after 7 days in these organ DNAs (data not shown). Additionally, with intragastric administration, no 4-OHE–DNA adducts were detected in the liver and kidney DNA (data not shown). In separate, independent mice experiments with the same 4-OHE dose, dC*, dG*, and 5-Me-dC* were also detected in the esophagus DNA in the range of 5.1 ± 5.9, 2.7 ± 0.7, and 1.0 ± 1.2 adducts per $10^8$ bases ($n = 3-4$), respectively.

**4-OHE Adduct Analysis in Human Lung DNA.** An LC/MS/MS method was used to detect 4-OHE adducts in human lung DNA (Figure 7). dC* was detected in all lung tissues, in the range of 2.6–5.9/$10^9$ bases, while dA* was detected in three samples (Table 6). dG* and 5-Me-dC* were not detected. The mean dC* and dA* levels in DNA were 4.04 and 1.75/$10^9$ bases, respectively. The levels of dC* and dA* did not significantly correlate with cigarette smoking or aging. These results suggested that 4-OHE–DNA adducts are commonly present in human lung tissue and may be useful as endogenous biomarkers of oxidative stress. However, to establish its presence in human lung tissue unambiguously, the peak attributed to dC* in the chromatogram should be confirmed by monitoring a second product ion and carefully confirming the retention times and the relative peak heights of the two products ions, as compared to a dC* standard.

## Discussion

This is the first report of the in vivo detection and quantification of 4-OHE–DNA adducts using an LC/MS/MS method. As described in the introduction, 4-OHE is mutagenic and is commonly present in our food, as a lipid oxidation product. Because dietary habits are a major factor in human carcinogenesis (*18*), the relation between the intake of 4-OHE via food

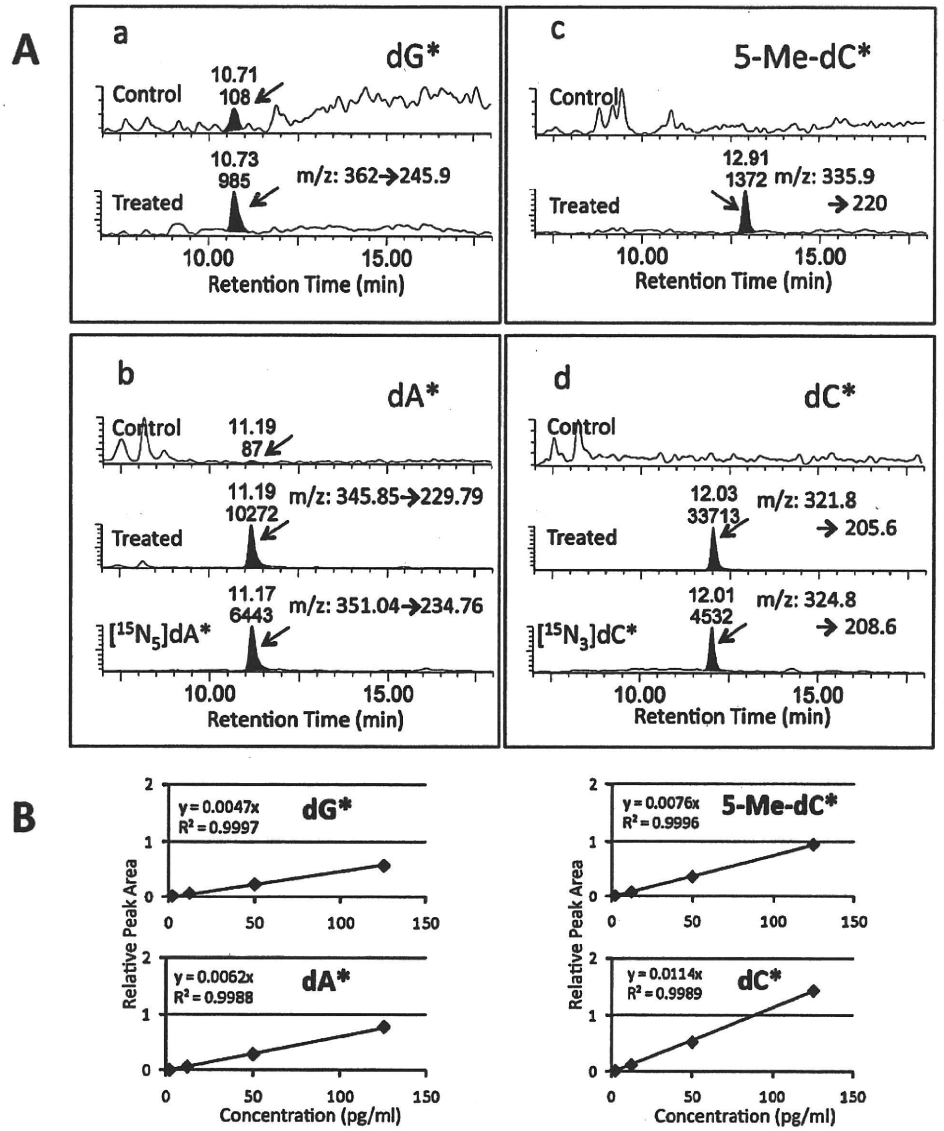


**Figure 6.** (A) LC/MS/MS analysis of 4-OHE−DNA adducts formed in mouse stomach. LC/ESI-MS/MS chromatograms of 4-OHE adducts and internal standards detected in mouse stomach DNA isolated from control- and 4-OHE-treated mice. Retention time (upper) and peak area (lower) are shown above each peak. (a) dG*, (b) dA*, (c) 5-Me-dC*, and (d) dC*. (B) Calibration curves for dG*, dA*, 5-Me-dC*, and dC*.

and carcinogenicity must be examined. So far, long-term carcinogenicity studies on 4-OHE have not been reported; however, as described in the Results, 4-OHE, like other carcinogenic α,β-unsaturated carbonyl compounds, such as acrolein or crotonaldehyde, forms DNA adducts in vivo.

The oral administration route of 4-OHE in mice resulted in DNA adduct formation in the digestive tract, for example, esophagus, stomach, and large intestine, but not in liver and kidney. It seems that the 4-OHE was directly absorbed after the i.g. administration by the esophageal, stomach, and large intestine tissues but was not distributed into the liver. The adduct distribution in the organs demonstrates a tendency of formation at the site of first contact with 4-OHE. The adduct levels decreased continuously during 7 days after administration (data not shown). The 4-OHE−DNA adducts might be repaired to a certain extent; however, the decrease in the adduct level can also be explained, at least in part, by cell turnover.

The formation of 4-hydroxy-2-nonenal and 4-oxo-2-nonenal (4-ONE) by ω-6 lipid peroxidation in biological systems and their adduct formation with proteins and DNA have been well-studied,

**Table 5. Levels of 4-OHE−DNA Adducts in Mouse Organs**[a]

| | | | | adducts/$10^8$ bases | | | |
|---|---|---|---|---|---|---|---|
| | | mg/mouse | h after treatment | dC* | dA* | dG* | 5-Me-dC* |
| stomach | control | 0 | 24 | ND | 0.3 ± 0.7 | 0.2 ± 0.3 | ND |
| | 4-OHE | 3 | 24 | 43.7 ± 24.7 | 30.2 ± 33.2 | 5.5 ± 3.2 | 3.4 ± 5.5 |
| | 4-OHE | 3 | 72 | 2.3 ± 2.6 | | 0.6 ± 0.6 | ND |
| large intestine | control | 0 | 24 | ND | 0.2 ± 0.4 | 0.1 ± 0.3 | ND |
| | 4-OHE | 3 | 24 | 5.6 ± 6.5 | 3.0 ± 3.4 | 1.0 ± 1.2 | 0.3 ± 0.7 |
| | 4-OHE | 3 | 72 | 0.5 ± 1.2 | | 0.2 ± 0.3 | ND |

[a] Data represent the mean ± SD; $n$ = 6−8.

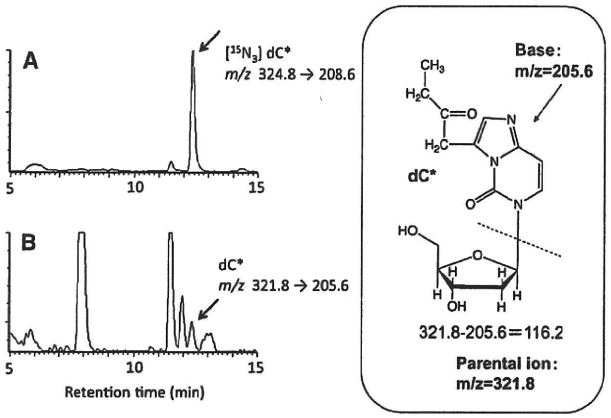


**Figure 7.** LC/MS/MS analysis of 4-OHE–DNA adducts in human lung DNA. (A) Analysis of $^{15}$N-dC*. The transition *m/z* 324.8→208.6 was monitored. (B) Analysis of dC*. The transition *m/z* 321.8→205.6 was monitored. A smoothing method was employed to improve the S/N value.

**Table 6. Levels of 4-OHE–DNA Adducts in Human Lung DNA**[a]

| | | | | adducts/10$^9$ bases | |
|---|---|---|---|---|---|
| patient | sex | age | smoking (BI) | dC* | dA* |
| 1 | male | 52 | 1280 | 3.6 | ND |
| 2 | male | 65 | 585 | 4.9 | 4.6 |
| 3 | male | 77 | 1500 | 3.7 | ND |
| 4 | male | 79 | 1160 | 5.9 | 3.9 |
| 5 | female | 56 | 0 | 3.3 | ND |
| 6 | female | 65 | 0 | 3.8 | ND |
| 7 | female | 70 | 0 | 4.4 | ND |
| 8 | female | 70 | 25 | 2.6 | 9.0 |
| 9 | female | 71 | 0 | 4.7 | ND |
| 10 | female | 76 | 0 | 3.5 | ND |

[a] dG* and 5-Me-dC* were not detected. BI, Brinkman index.

as markers of endogenous oxidative stress in relation to lipid peroxidation (*4*, *22*). For example, 4-hydroxy-2-nonenal–protein adducts have been found in the lung tissues from patients with chronic pulmonary disease (*23*). Blair and his collaborators detected a 4-ONE adduct with glutathione and suggested that it is a good marker of cellular oxidative stress (*24*). Our discovery of 4-OHE has two important implications: (1) It may be a food mutagen produced during cooking or storage; for example, fried fish and old cooking oil contain large amounts of 4-OHE; and (2) it may also be an endogenous mutagen produced by lipid peroxidation in membranes in vivo. Protein-bound forms of an $\omega$-3 lipid peroxidation product, 4-hydroxy-2-hexenal, were detected in the liver tissues from patients with chronic hepatitis C (*25*). In the present study, we detected dC* clearly in all of the human lung DNA samples. Therefore, 4-OHE–DNA adducts may be useful markers of environmental exposure to 4-OHE and endogenous oxidative stress in relation to cancer induction.

**Acknowledgment.** This work was supported by grants from the Ministry of Health, Labor and Welfare of Japan.

**Supporting Information Available:** $^1$H–$^{13}$C HMBC spectrum of 5-Me-dC*, $^1$H–$^{15}$N HMBC spectrum of 5-Me-dC*, $^1$H–$^{15}$N HMBC spectrum of dA*, and mass spectra of dC*, 5-Me-dC*, and dA* obtained by HRESI-MS/MS analyses. This material is available free of charge via the Internet at http://pubs.acs.org.

## References

(1) Esterbauer, H. (1993) Cytotoxicity and genotoxicity of lipid-oxidation products. *Am. J. Clin. Nutr. 57*, S779–S786.

(2) Esterbauer, H., Schaur, R. J., and Zollner, H. (1991) Chemistry and biochemistry of 4-hydroxynonenal, malonaldehyde and related aldehydes. *Free Radical Biol. Med. 11*, 81–128.

(3) Chung, F. L., Young, R., and Hecht, S. S. (1984) Formation of cyclic adducts of 1,$N^2$propanodeoxyguanosine adducts in DNA upon reaction with acrolein or crotonaldehyde. *Cancer Res. 44*, 990–995.

(4) Blair, I. A. (2001) Lipid hydroperoxide-mediated DNA damage. *Exp. Gerontol. 36*, 1473–1481.

(5) Cajelli, E., Ferraris, A., and Brambilla, G. (1987) Mutagenicity of 4-hydroxynonenal in V79 Chinese hamster cells. *Mutat. Res. 190*, 169–171.

(6) Marnett, L. J., Hurd, H. K., Hollstein, M. C., Levin, D. E., Esterbauer, H., and Ames, B. N. (1985) Naturally occurring carbonyl compounds are mutagens in Salmonella tester strain TA104. *Mutat. Res. 148*, 25–34.

(7) Shields, P. G., Xu, G. X., Blot, W. J., Fraumeni, J. F., Trivers, G. E., Pellizzari, E. D., Qu, Y. H., Gao, Y. T., and Harris, C. C. (1995) Mutagens from heated Chinese and U.S. cooking oils. *J. Natl. Cancer Inst. 87*, 836–841.

(8) Fujioka, K., and Shibamoto, T. (2006) Determination of toxic carbonyl compounds in cigarette smoke. *Environ. Toxicol. 21*, 47–54.

(9) Burcham, P. C. (1999) Internal hazards: Baseline DNA damage by endogenous products of normal metabolism. *Mutat. Res., Genet. Toxicol. Environ. Mutagen. 443*, 11–36.

(10) Kasai, H., Maekawa, M., Kawai, K., Hachisuka, K., Takahashi, Y., Nakamura, H., Sawa, R., Matsui, S., and Matsuda, T. (2005) 4-oxo-2-hexenal, a mutagen formed by omega-3 fat peroxidation, causes DNA adduct formation in mouse organs. *Ind. Health 43*, 699–701: ibid; 46, 101, 2008.

(11) Maekawa, M., Kawai, K., Takahashi, Y., Nakamura, H., Watanabe, T., Sawa, R., Hachisuka, K., and Kasai, H. (2006) Identification of 4-oxo-2-hexenal and other direct mutagens formed in model lipid peroxidation reactions as dGuo adducts. *Chem. Res. Toxicol. 19*, 130–138.

(12) Kawai, K., Matsuno, K., and Kasai, H. (2006) Detection of 4-oxo-2-hexenal, a novel mutagenic product of lipid peroxidation, in human diet and cooking vapor. *Mutat. Res. 603*, 186–192.

(13) Kasai, H., and Kawai, K. (2008) 4-oxo-2-hexenal, a mutagen formed by omega-3 fat peroxidation: Occurrence, detection and adduct formation. *Mutat. Res., Rev. Mutat. Res. 659*, 56–59.

(14) Rindgen, D., Nakajima, M., Wehrli, S., Xu, K. Y., and Blair, I. A. (1999) Covalent modifications to 2′-deoxyguanosine by 4-oxo-2-nonenal, a novel product of lipid peroxidation. *Chem. Res. Toxicol. 12*, 1195–1204.

(15) Lee, S. H., Rindgen, D., Bible, R. H., Hajdu, E., and Blair, I. A. (2000) Characterization of 2′-deoxyadenosine adducts derived from 4-oxo-2-nonenal, a novel product of lipid peroxidation. *Chem. Res. Toxicol. 13*, 565–574.

(16) Pollack, M., Oe, T., Lee, S. H., Elipe, M. V. S., Arison, B. H., and Blair, I. A. (2003) Characterization of 2′-deoxycytidine adducts derived from 4-oxo-2-nonenal, a novel lipid peroxidation product. *Chem. Res. Toxicol. 16*, 893–900.

(17) Kawai, Y., Uchida, K., and Osawa, T. (2004) 2′-Deoxycytidine in free nucleosides and double-stranded DNA, as the major target of lipid peroxidation products. *Free Radical Biol. Med. 36*, 529–541.

(18) Sugimura, T. (2002) Food and cancer. *Toxicology 181*, 17–21.

(19) Wang, T. J., Zhou, B. S., and Shi, J. P. (1996) Lung cancer in nonsmoking Chinese women: A case-control study. *Lung Cancer 14*, S93–S98.

(20) Zhong, L. J., Goldberg, M. S., Gao, Y. T., and Jin, F. (1999) Lung cancer and indoor air pollution arising from Chinese style cooking among nonsmoking women living in Shanghai, China. *Epidemiology 10*, 488–494.

(21) Matsuda, T., Yabushita, H., Kanaly, R. A., Shibutani, S., and Yokoyama, A. (2006) Increased DNA damage in ALDH2-deficient alcoholics. *Chem. Res. Toxicol. 19*, 1374–1378.

(22) Douki, T., Odin, F., Caillat, S., Favier, A., and Cadet, J. (2004) Predominance of the 1, $N^2$propano 2′-deoxyguanosine adduct among 4-hydroxy-2-nonenal-induced DNA lesions. *Free Radical Biol. Med. 37*, 62–70.

(23) Rahman, I., van Schadewijk, A. A. M., Crowther, A. J. L., Hiemstra, P. S., Stolk, J., MacNee, W., and De Boer, W. I. (2002) 4-Hydroxy-2-nonenal, a specific lipid peroxidation product, is elevated in lungs of patients with chronic obstructive pulmonary disease. *Am. J. Respir. Crit. Care Med. 166*, 490–495.

(24) Blair, I. A. (2006) Endogenous glutathione adducts. *Curr. Drug Metab. 7*, 853–872.

(25) Kitase, A., Hino, K., Furutani, T., Okuda, M., Gondo, T., Hidaka, I., Hara, Y., Yamaguchi, Y., and Okita, K. (2005) In situ detection of oxidized n-3 polyunsaturated fatty acids in chronic hepatitis C: Correlation with hepatic steatosis. *J. Gastroenterol. 40*, 617–624.

TX9003819

# Detection of Lipid Peroxidation-Induced DNA Adducts Caused by 4-Oxo-2(*E*)-nonenal and 4-Oxo-2(*E*)-hexenal in Human Autopsy Tissues

Pei-Hsin Chou,[†,‡] Shinji Kageyama,[§] Shun Matsuda,[†] Keishi Kanemoto,[†] Yoshiaki Sasada,[†] Megumi Oka,[†] Kazuya Shinmura,[§] Hiroki Mori,[§] Kazuaki Kawai,[∥] Hiroshi Kasai,[∥] Haruhiko Sugimura,*[,§] and Tomonari Matsuda*[,†]

*Research Center for Environmental Quality Management, Kyoto University, Otsu, Shiga, 520-0811, Japan, Department of Environmental Engineering, National Cheng Kung University, Tainan, 70101, Taiwan, Department of Pathology, Hamamatsu University School of Medicine, Hamamatsu, Shizuoka, 431-3192, Japan, and Department of Environmental Oncology, University of Occupational and Environmental Health, Kitakyushu, Fukuoka, 807-8555, Japan*

*Received February 8, 2010*

DNA adducts are produced both exogenously and endogenously via exposure to various DNA-damaging agents. Two lipid peroxidation (LPO) products, 4-oxo-2(*E*)-nonenal (4-ONE) and 4-oxo-2(*E*)-hexenal (4-OHE), induce substituted etheno-DNA adducts in cells and chemically treated animals, but the adduct levels in humans have never been reported. It is important to investigate the occurrence of 4-ONE- and 4-OHE-derived DNA adducts in humans to further understand their potential impact on human health. In this study, we conducted DNA adductome analysis of several human specimens of pulmonary DNA as well as various LPO-induced DNA adducts in 68 human autopsy tissues, including colon, heart, kidney, liver, lung, pancreas, small intestine, and spleen, by liquid chromatography tandem mass spectrometry. In the adductome analysis, DNA adducts derived from 4-ONE and 4-OHE, namely, heptanone-etheno-2′-deoxycytidine (HεdC), heptanone-etheno-2′-deoxyadenosine (HεdA), and butanone-etheno-2′-deoxycytidine (BεdC), were identified as major adducts in one human pulmonary DNA. Quantitative analysis revealed 4-ONE-derived HεdC, HεdA, and heptanone-etheno-2′-deoxyguanosine (HεdG) to be ubiquitous in various human tissues at median values of 10, 15, and 8.6 adducts per $10^8$ bases, respectively. More importantly, an extremely high level (more than 100 per $10^8$ bases) of these DNA adducts was observed in several cases. The level of 4-OHE-derived BεdC was highly correlated with that of HεdC ($R^2 = 0.94$), although BεdC was present at about a 7-fold lower concentration than HεdC. These results suggest that 4-ONE- and 4-OHE-derived DNA adducts are likely to be significant DNA adducts in human tissues, with potential for deleterious effects on human health.

## Introduction

Lipid peroxidation (LPO[1]) is a major source of DNA-damaging agents. Decomposition products generated from the LPO of polyunsaturated fatty acids (PUFAs) are highly DNA-reactive, including acrolein, crotonaldehyde, malondialdehyde, and other α,β-unsaturated aldehydes (*1–3*). These electrophilic aldehydes may modify nucleic acid bases to form DNA adducts implicated in mutagenesis, carcinogenesis, accelerated aging, or neurological deterioration (*4–6*). Thus, investigation into the levels and tissue distributions of LPO-derived DNA adducts in humans is important to further understand their possible impact on human health.

LPO-related DNA adducts identified in human tissues are mainly exocyclic etheno and propano adducts such as 1,$N^6$-etheno-2′-deoxyadenosine (εdA); 3,$N^4$-etheno-2′-deoxycytidine (εdC); 1, $N^2$-propano-2′-deoxyguanosines generated from acrolein, crotonaldehyde, and 4-hydroxy-2(*E*)-nonenal (4-HNE); and malondialdehyde-derived 3-(2-deoxy-β-D-erythro-pentofuranosyl)pyrimido[1,2-α]purin-10(3*H*)-one (*7–9*). The long-chain aldehyde 4-HNE is an ω-6 PUFA-peroxidation product that reacts with DNA and protein (*10–12*); furthermore, 4-HNE-related DNA adducts have been reported to be associated with carcinogenesis and Alzheimer's disease (*13–15*). 4-Oxo-2(*E*)-nonenal (4-ONE), another decomposition product of ω-6 PUFAs, has also been shown to induce the formation of etheno DNA adducts carrying aliphatic side chains both in cells and in mouse models, including heptanone-etheno-2′-deoxycytidine (HεdC), heptanone-etheno-2′-deoxyguanosine (HεdG), and heptanone-etheno-2′-deoxyadenosine (HεdA) (*16–18*). 4-Oxo-2(*E*)-hexenal (4-OHE), an ω-3 PUFA-peroxidation product having a chemical structure similar to that of 4-ONE, was recently reported to be able to produce etheno DNA adducts as well,

* Corresponding author. (H.S. (for medical questions)) E-mail: hsugimur@hama-med.ac.jp. (T.M. (for DNA adduct analysis)) E-mail: matsuda@z05.mbox.media.kyoto-u.ac.jp.

[†] Kyoto University.

[‡] National Cheng Kung University.

[§] Hamamatsu University School of Medicine.

[∥] University of Occupational and Environmental Health.

[1] Abbreviations: PUFA, polyunsaturated fatty acid; LPO, lipid peroxidation; 4-HNE, 4-hydroxy-2(*E*)-nonenal; 4-ONE, 4-oxo-2(*E*)-nonenal; 4-OHE, 4-oxo-2(*E*)-hexenal; HεdC, heptanone-etheno-2′-deoxycytidine; HεdG, heptanone-etheno-2′-deoxyguanosine; HεdA, heptanone-etheno-2′-deoxyadenosine; BεdC, butanone-etheno-2′-deoxycytidine; BεmedC, butanone-etheno-2′-deoxy-5-methylcytidine; BεdG, butanone-etheno-2′-deoxyguanosine; BεdA, butanone-etheno-2′-deoxyadenosine; 8-oxodG, 8-oxo-7,8-dihydro-2′-deoxyguanosine; εdA, 1,$N^6$-etheno-2′-deoxyadenosine; 8-OHAdG, 8-hydroxy-1,$N^2$-propanodeoxyguanosine; $CdG_2$, α-*R*-methyl-γ-hydroxy-1,$N^2$-propano-2′-deoxyguanosine;COX-2, cyclooxygenase-2; HPNE, 4-hydroperoxy-2(*E*)-nonenal; EDE, 4,5-epoxy-2(*E*)-decenal; 5-LO, 5-lipoxygenase.

10.1021/tx100047d 

such as butanone-etheno-2′-deoxycytidine (BεdC), butanone-etheno-2′-deoxy-5-methyl-cytidine (BεmedC), butanone-etheno-2′-deoxyguanosine (BεdG) (*19–21*), and butanone-etheno-2′-deoxyadenosine (BεdA) (*22*). The levels of 4-ONE- and 4-OHE-related DNA adducts in humans are currently unknown because such adducts were discovered only very recently.

In addition to LPO-derived DNA adducts, various other types of DNA lesions are frequently formed in humans as a consequence of exposure to environmental carcinogens or endogenous DNA-reactive agents. Because a variety of DNA adducts are present in human tissues, comprehensive investigation of these base modifications is necessary to identify the ones most critical to mutagenesis and carcinogenesis in humans. Recently, we developed a novel technique to detect multiple known or unknown DNA adducts simultaneously by using LC-MS/MS (*23, 24*). This approach, named the DNA adductome approach, monitors the neutral loss of 2′-deoxyribose from positively ionized 2′-deoxynucleoside adducts over a certain range of transitions. A variety of DNA adducts detected in DNA samples can be presented and compared by creating an adductome map showing LC retention time, mass-to-charge ratio (*m/z*), and relative peak intensity of each potential DNA adduct. In this study, we applied the DNA adductome approach to several human pulmonary DNA specimens and identified major DNA adducts on the adductome maps. Interestingly, 4-ONE- and 4-OHE-related DNA adducts were found to be major adducts in at least one pulmonary DNA sample, and they were also detected in other DNA samples. We also analyzed the levels of 4-ONE- and 4-OHE-related DNA adducts in various organs of different individuals by using LC-MS/MS. The lesions were found to be widely distributed, with some being present in significant amounts, suggesting that they could be important causative factors in human disease.

## Experimental Procedures

**Human Autopsy Tissues.** Human autopsy tissue samples were collected at Hamamatsu University School of Medicine, Japan, and the study design was approved by the Institutional Review Board of Hamamatsu University School of Medicine (18−4). Sixty-eight samples were obtained from organs of 26 deceased persons, including the colon ($n = 6$), liver ($n = 19$), lung ($n = 12$), pancreas ($n = 9$), spleen ($n = 9$), kidney ($n = 9$), heart ($n = 2$), and small intestine ($n = 2$). The samples were taken within 24 h after death and frozen at −80 °C until DNA extraction. The ages of the subjects (17 males and 9 females) ranged from 26 to 90. Seventeen of them had malignancies as backgrounds, and final remarkable circulatory failures (shock, massive hemorrhage, and sepsis) were validated both clinically and pathologically in 6 cases. Detailed properties of the patients are listed in Supporting Information, Table S-1.

**DNA Adduct Standards and Stable Isotope Standards.** 4-ONE- and 4-OHE-related DNA adducts (HεdC, HεdA, HεdG, BεdC, BεmedC, BεdA, and BεdG) were synthesized according to previously published methods (*16–20*). The stereoisomers α-*S*- and α-*R*-methyl-γ-hydroxy-1,$N^2$-propano-2′-deoxyguanosine ($CdG_1$, $CdG_2$), 8-hydroxy-1,$N^2$-propanodeoxyguanosine (8-OH-AdG), and the two stereoisomers of 6-hydroxy-1,$N^2$-propanodeoxyguanosine (6-OH-$AdG_1$ and 6-OH-$AdG_2$) were prepared as previously described (*24*). 8-OxodG and εdA were obtained from Sigma Aldrich Japan (Japan). [U-$^{15}N_5$]-8-oxodG was kindly provided by Dr. Shinya Shibutani, State University of New York, Stony Brook, NY, [$^{15}N_5$, $^{13}C_{10}$]-2-(2′-deoxyguanosine-8-yl)-3-aminobenzanthrone ([$^{15}N_5$, $^{13}C_{10}$]-C8-C2-ABA) was kindly provided by Dr. Takeji Takamura, Kanagawa Institute of Technology, Japan, and other DNA adduct stable isotope standards were synthesized according to previously described methods using [U-$^{15}N_5$]- or [U-$^{15}N_3$]-deoxynucleosides purchased from Cambridge Isotope Laboratories (Andover, MA).

**DNA Purification and Hydrolysis.** Genomic DNA was isolated and purified from human autopsy samples by using a Gentra Puregene Tissue Kit (QIAGEN, Valencia, CA). DNA extraction was undertaken according to the protocol provided by the manufacturer, with the addition of desferroxamine to all solutions to a final concentration of 0.1 mM.

For DNA adductome analysis, isolated DNA was enzymatically digested as follows: each DNA sample (100 μg) was mixed with 54 μL of digestion buffer (17 mM sodium succinate and 8 mM calcium chloride, pH 6.0) containing 67.5 units of micrococcal nuclease (Worthington, Lakewood, NJ) and 0.255 units of spleen phosphodiesterase (Worthington, Lakewood, NJ). After 3 h of incubation at 37 °C, 3 units of alkaline phosphatase (Sigma-Aldrich, St. Louis, MO), 30 μL of 0.5 M Tris-HCl (pH 8.5), 15 μL of 20 mM zinc sulfate, and 101 μL of Milli-Q water were added, and the mixture were incubated for another 3 h at 37 °C. After this incubation, the mixture was concentrated to 10−20 μL by a Speed-Vac concentrator, and 100 μL of methanol was added to precipitate the protein. After centrifugation, the methanol fraction (supernatant) was transferred to a new Eppendorf tube. The precipitate was extracted with 100 μL of methanol, and the methanol fractions were combined and evaporated to dryness.

For adduct quantification analysis, the DNA sample (50 μg) was mixed with 18 μL of digestion buffer (17 mM sodium succinate and 8 mM calcium chloride, pH 6.0) containing 22.5 units of micrococcal nuclease (Worthington, Lakewood, NJ) and 0.075 units of spleen phosphodiesterase (Worthington, Lakewood, NJ) and 10 units of stable isotope-labeled DNA adduct internal standards mix, including 27.8 nM [U-$^{15}N_5$]-8-oxodG, and 1.1 nM [U-$^{15}N_5$]-εdA, [U-$^{15}N_5$]-$CdG_1$, [U-$^{15}N_5$]-$CdG_2$, [U-$^{15}N_5$]-8-OH-AdG, [U-$^{15}N_3$]-HεdC, [U-$^{15}N_5$]-HεdA, [U-$^{15}N_5$]-HεdG, [U-$^{15}N_3$]-BεdC, and [U-$^{15}N_5$]-BεdA. After 3 h of incubation at 37 °C, 3 units of alkaline phosphatase (Sigma-Aldrich, St. Louis, MO), 10 μL of 0.5 M Tris-HCl (pH 8.5), 5 μL of 20 mM zinc sulfate, and 67 μL of Milli-Q water were added, and the mixture were incubated for another 3 h at 37 °C. After this incubation, the mixture was concentrated to 10−20 μL by a Speed-Vac concentrator, and 100 μL of methanol was added to precipitate the protein. After centrifugation, the methanol fraction (supernatant) was transferred to a new Eppendorf tube. The precipitate was extracted with 100 μL of methanol, and the methanol fractions were combined and evaporated to dryness.

**DNA Adductome Analysis.** Digested DNA used for adductome analysis was redissolved in 120 μL of 30% dimethyl sulfoxide containing 23 nM [$^{15}N_5$, $^{13}C_{10}$]-C8-C2-ABA as the internal standard and then subjected to DNA adductome analysis similar to that described by Kanaly et al. (*24*). Briefly, adductome analysis was carried out using a Quattro Ultima Pt triple stage quadrupole mass spectrometer (Waters-Micromass, Milford, MA) equipped with a Shimadzu LC system (Shimadzu, Japan). An aliquot of digested DNA sample (10 μL) was injected and separated by a Shim-pack XR-ODS column (3.0 mm × 75 mm, Shimadzu, Japan). The column was eluted in a linear gradient of 5% to 80% methanol in water from 0 to 40 min and kept in 80% methanol in water from 40 to 45 min at a flow rate of 0.2 mL/min. Multi-reaction monitoring (MRM) was performed in positive ion mode using nitrogen as the nebulizing gas. Experimental conditions were set as follows: ion source temperature, 130 °C; desolvation temperature, 380 °C; cone voltage, 35 V; collision energy, 15 eV; desolvation gas flow rate, 700 L/h; cone gas flow rate, 35 L/h; collision gas, argon. The strategy was designed to detect the neutral loss of 2′-deoxyribose from positively ionized 2′-deoxynucleoside adducts by monitoring the samples transmitting their $[M + H]^+ \rightarrow [M + H - 116]^+$ transitions. For each DNA sample, 241 MRM transitions were monitored over the *m/z* range from transition *m/z* 250 → 134 to transition 492 → 376. For each sample injection, a total of 31 channels were monitored simultaneously with one channel for each injection reserved to monitor the internal standard [$^{15}N_5$, $^{13}C_{10}$]-C8-C2-ABA at transition *m/z* 526 → 405. Each sample was injected 8 times to complete the monitoring of 241 MRM transitions. Transitions of normal deoxynucleosides, including 252 → 136 ([dA

+ H]$^+$) and 268 → 152 ([dG + H]$^+$), were not monitored in the adductome analysis.

Relative peak intensity of each potential DNA adduct was calculated as follows: (the peak area of the potential DNA adduct)/(the peak area of the internal standard)/(the amount of 2′-deoxyguanosine (dG)). The amount of dG in each DNA sample was estimated by monitoring the dG peak area at 254 nm using the Shimazu SPD-10Avp UV−visible detector connected in series with the LC/MS/MS. The relative peak intensity was plotted as a bubble chart in which the horizontal axis was retention time and the vertical axis is *m/z*. Sodium and potassium adducts of normal deoxynucleosides or other corresponding peaks, such as those detected in the retention times of 9.3−9.5 min (dC), 10.2−10.4 min (dG), 11.2−11.4 min (dT), and 14.0−14.2 min (dA), were not included in the plot.

**DNA Adduct Quantification.** The digested DNA sample used for quantification was resuspended in 50 μL of 30% dimethyl sulfoxide before LC-MS/MS analysis. An aliquot (20 μL) was injected and separated by the Shim-pack XR-ODS column, eluted in a linear gradient of 5% to 30% methanol in water from 0 to 27 min, 30% to 80% from 27 to 35 min, then kept in 80% from 35 to 40 min at a flow rate of 0.2 mL/min. For the quantification of 4-ONE-derived DNA adducts, HεdC, HεdG, and HεdA, another HPLC-gradient condition was employed because of the high hydrophobicity of these compounds. A remaining aliquot (20 μL) was injected and separated by the same column, eluted in a linear gradient of 45% to 90% methanol in water from 0 to 20 min at a flow rate of 0.2 mL/min. Experimental conditions were identical to those set for adductome analysis except that the cone voltage and collision energy were different for different DNA adducts. The collision energies and characteristic reactions monitored for the different DNA adducts are as follows (cone voltage (V), collision energy (eV), base ionS → product ion): [U-$^{15}N_5$]-8-oxodG (40, 12, 288.8 → 172.8), [U-$^{15}N_5$]-εdA (35, 14, 280.9 → 164.9), [U-$^{15}N_5$]-$CdG_1$ and [U-$^{15}N_5$]-$CdG_2$ (35, 10, 343.0 → 227.0), [U-$^{15}N_5$]-8-OH-AdG (35, 10, 329.3 → 213.3), [U-$^{15}N_3$]-HεdC (35, 10, 367.0 → 251.0), [U-$^{15}N_5$]-HεdA (35, 10, 393.0 → 277.0), [U-$^{15}N_5$]-HεdG (35, 10, 409.0 → 293.0), [U-$^{15}N_3$]-BεdC (35, 10, 324.8 → 208.6), and [U-$^{15}N_5$]-BεdA (35, 10, 351.0 → 234.8), 8-oxodG (40, 12, 283.8 → 167.8), εdA (35, 14, 275.9 → 159.9), $CdG_1$ and $CdG_2$ (35, 10, 338.0 → 222.0), 8-OH-AdG, 6-OH-$AdG_1$, and 6-OH-$AdG_2$ (35, 10, 324.3 → 208.3), HεdC (35, 10, 364.0 → 248.0), HεdA (35, 10, 388.0 → 272.0), HεdG (35, 10, 404.0 → 288.0), BεdC (35, 10, 321.8 → 205.6), BεmedC (35, 20, 335.9 → 220.0), and BεdA (35, 10, 351.0 → 234.8) and BεdG (35, 20, 362.0 → 245.9).

The amount of each DNA adduct was quantified by calculating the peak area ratio of the target DNA adduct and its specific internal standard ([U-$^{15}N_3$]-BεdC was used for BεdC and BεmedC, and [U-$^{15}N_5$]-BεdA was used for BεdA and BεdG). Calibration curves were obtained by using authentic standards spiked with isotope internal standards. The concentration of dG in each DNA sample was also monitored as described in the DNA Adductome Analysis section. The number of DNA adducts per $10^8$ bases was calculated by the following equation: number of DNA adducts per $10^8$ bases = adduct level (fmol/μmol dG) × 0.218(μmol dG/μmol dN) × $10^{-1}$, as described previously (*25*).

## Results

**Adductome Analysis of DNA Extracted from Human Lung Autopsy Tissues.** We applied adductome analysis to DNA extracted from four human lung autopsy samples to simultaneously detect a variety of known and unknown DNA adducts in human pulmonary DNA. Although adductome analysis is semiquantitative, this analysis would help to grasp a complete picture of the DNA adducts in human samples. Several peaks were identified as corresponding to known DNA adducts by showing identical *m/z* and LC retention times to DNA adduct standards. Figure 1 shows the adductome maps of two human pulmonary DNA samples having different patterns of DNA adduct composition. Numerous DNA adducts can be seen in Figure 1A, and LPO-induced DNA adducts were detected as major peaks, including HεdC, HεdA, BεdC, BεdA, BεmedC, BεdG, εdA, and 1,$N^2$-glyoxal-dG. Although fewer DNA adducts were found in the sample represented in Figure 1B, LPO-induced DNA adducts derived from 4-ONE and 4-OHE (i.e., HεdC, HεdA, and BεdC) were nonetheless detected. Adductome maps of two other human pulmonary DNA samples have patterns similar to that shown in Figure 1B (data not shown),

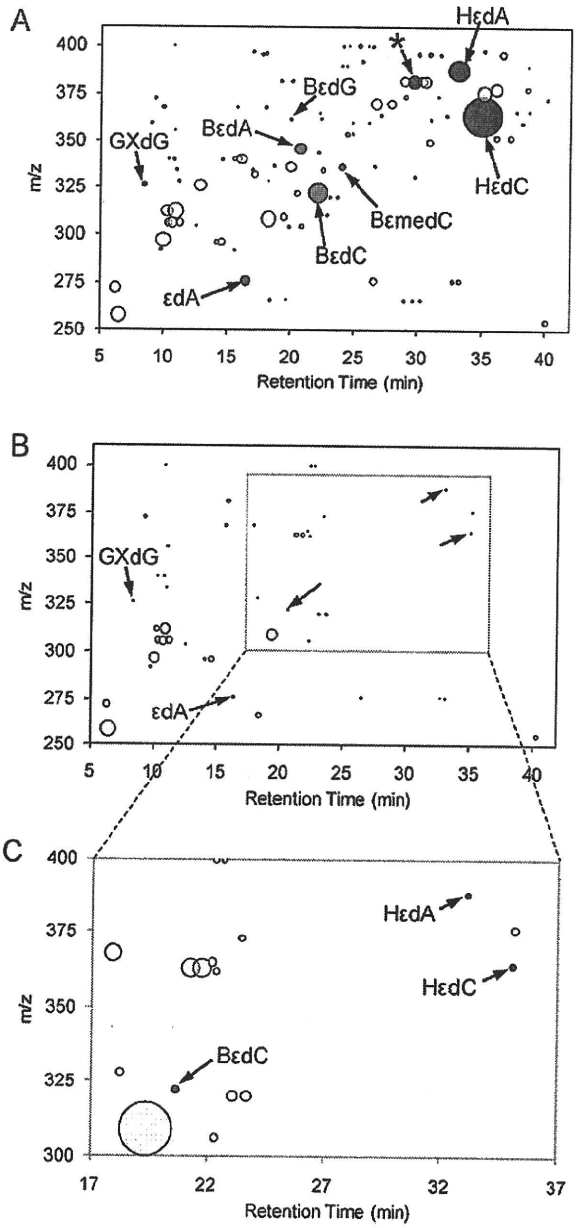


**Figure 1.** A and B show the DNA adductome maps of two human pulmonary DNA samples from different individuals, and C is a close-up of a selected area in B. Each circle represents one DNA adduct candidate detected by adductome analysis using LC-MS/MS. HPLC retention time, mass to charge ratio (*m/z*), and relative intensity (shown by the size of each circle, which is proportional to the peak area of each DNA adduct candidate divided by the peak area of the internal standard and the amount of 2′-deoxyguanosine) of each DNA adduct candidate can be found on the maps. Blue circles represent corresponding peaks of 4-ONE-related DNA adducts, while orange circles represent 4-OHE-related DNA adducts. Green circles are the other lipid-peroxidation derived DNA adducts, and yellow circles represent unidentified peaks. GXdG: 1,$N^2$-glyoxyal-dG. *: heptanone-ethano-2′-deoxycytidine.

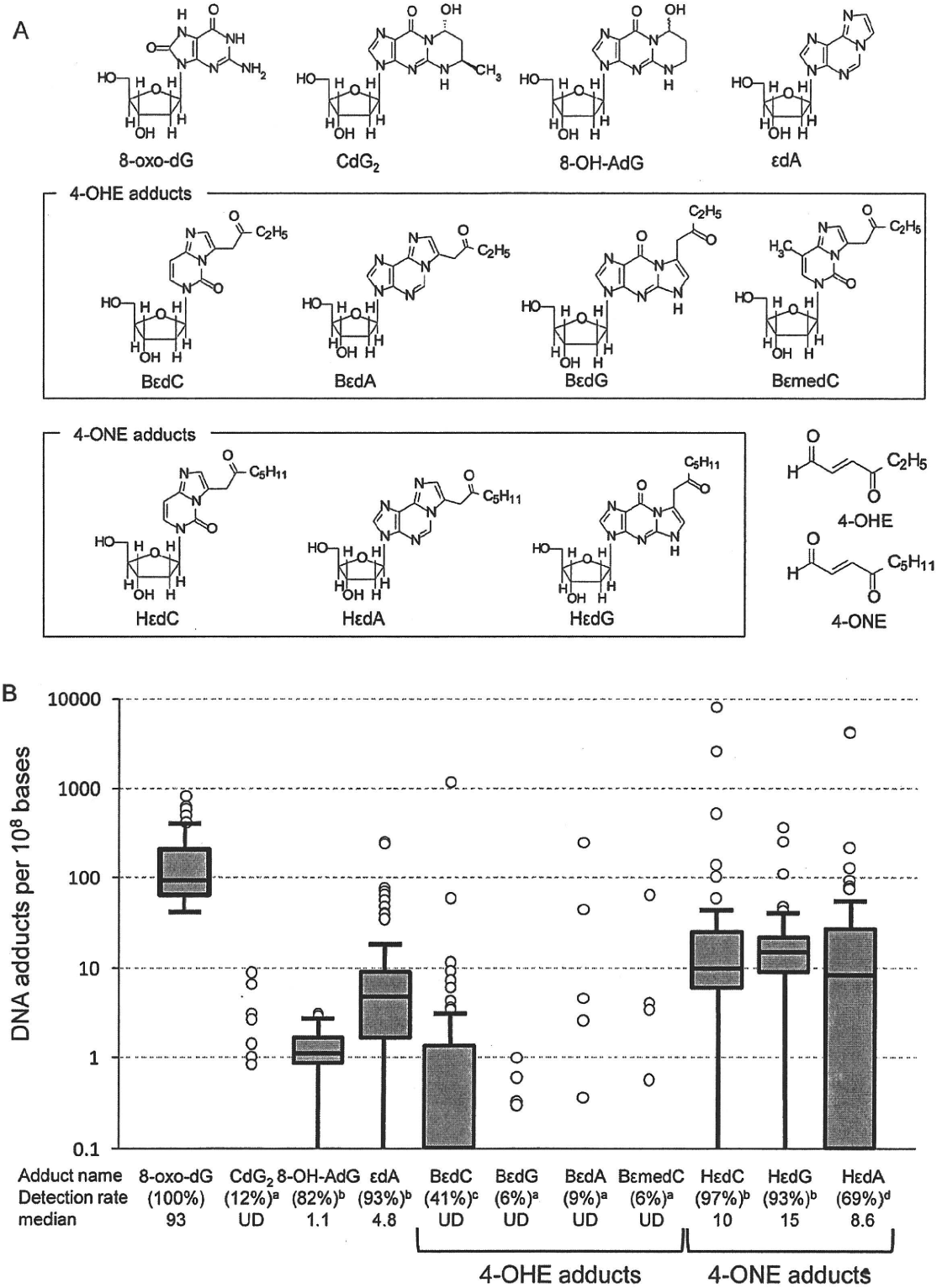


**Figure 2.** Level of LPO-induced DNA adducts in human tissues. (A) Chemical structure of DNA adducts detected in human tissues and the chemical structure of 4-OHE and 4-ONE. (B) Box-whisker plot of the levels of DNA adducts detected in human autopsy tissues, including the colon, liver, lung, pancreas, spleen, kidney, heart, and small intestine ($n$ = 68). The boxes indicate the 75th percentile, the median, and the 25th percentile. The ends of the whiskers indicate the minimum and maximum data values unless outliers are present, in which case the whiskers extend to a maximum of 1.5 times the interquartile range. Circles above the whisker indicate outliers. Although crotonaldehyde-induced $CdG_1$ and acrolein-induced 6-OH-$AdG_1$ and 6-OH-$AdG_2$ were also monitored, we could not detect those adducts. Detected rate and median are shown under each DNA adduct. UD: under the detection limit. a, 75th percentile was UD; b, minimum was UD; c, median was UD; d, 25th percentile was UD.

indicating that DNA adducts induced by 4-ONE and 4-OHE are often formed in human lungs.

**Detection of 4-ONE- and 4-OHE-Induced DNA Adducts in Human Autopsy Tissues.** To elucidate whether the levels of

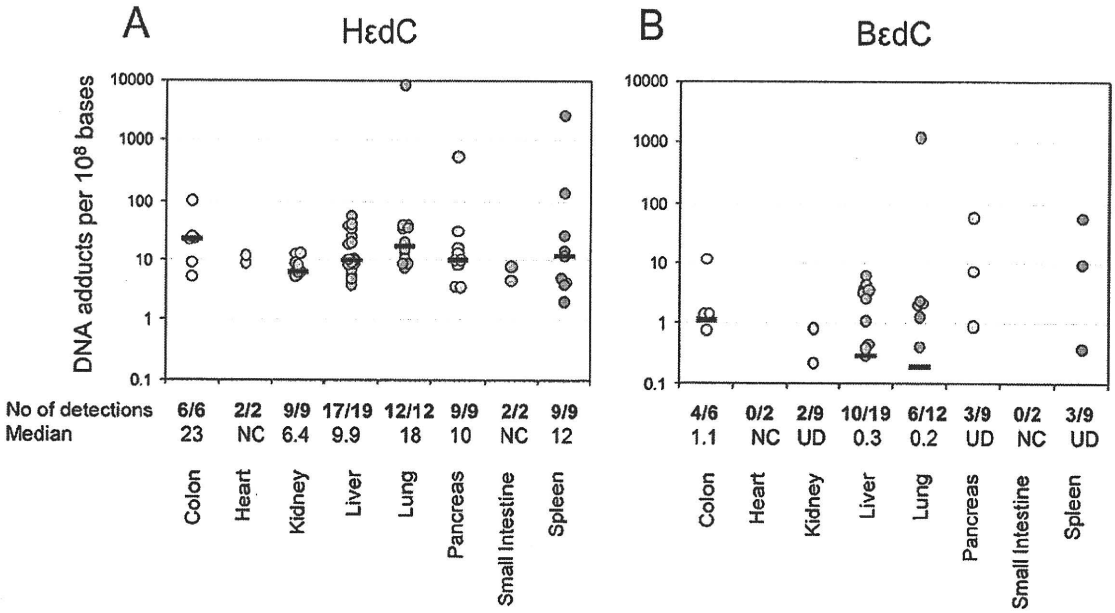


**Figure 3.** DNA adduct levels of HεdC and BεdC detected in various human autopsy tissues. Data from the DNA of 6 colons, 2 hearts, 9 kidneys, 19 livers, 12 lungs, 9 pancreases, 2 small intestines, and 9 spleens were plotted as circles, and the blue bars indicate the median values. NC: not calculated because the sample number was only 2. UD: median was under the detection limit.

4-ONE- and 4-OHE-related DNA adducts are comparable to those of other DNA adducts frequently found in human tissues, we measured the levels of various DNA adducts by using LC-MS/MS in 68 human autopsy specimens obtained from 26 persons, including samples of colon ($n$ = 6), liver ($n$ = 19), lung ($n$ = 12), pancreas ($n$ = 9), spleen ($n$ = 9), kidney ($n$ = 9), heart ($n$ = 2), and small intestine ($n$ = 2). The approximate detection limit of the DNA adducts (in the case that 50 $\mu$g of DNA was digested and 40% of the portion was injected to the LC/MS/MS) were as follows: 8-oxodG (1.65 adduct per $10^8$ bases), εdA (0.17), $CdG_1$ and $CdG_2$ (0.17), 8-OH-AdG (0.05), 6-OH-$AdG_1$ and 6-OH-$AdG_2$ (0.08), HεdC (0.33), HεdA (1.65), HεdG (1.65), BεdC (0.17), BεmedC (0.17), and BεdA (0.83) and BεdG (0.83) (Supporting Information Figures S-2 and S-3, Table S-8), and the calibration curves of each DNA adducts are shown in Supporting Information, Figure S-4. We could detect the target DNA adducts in several human tissue samples (the representative chromatographs are shown in Supporting Information, Figures S-5, S-6, and S-7). The results revealed that the levels of target DNA adducts varied considerably among individuals or organs (Figure 2 and Supporting Information, Table S-8). Figure 2 shows the DNA adduct levels of the oxidative lesion 8-oxodG as well as the LPO-related lesions $CdG_2$, 8-OH-AdG, εdA, BεdC, BεdG, BεdA, BεmedC, HεdC, HεdG, and HεdA. 8-OxodG was detected in all autopsy tissues, and high detection rates were also found for εdA (93%) and 8-OH-AdG (82%). 4-ONE-related DNA adducts were also frequently detected in various tissue samples: total detection rates for HεdC, HεdG, and HεdA were 97%, 93%, and 63%, respectively. 4-OHE-related BεdC, having a total detection rate of 41%, was commonly found in the colon, liver, and lung, with detection rates higher than 50%. However, the other 4-OHE-related adducts, BεdG, BεdA, and BεmedC, showed lower detection rates of 6%, 9%, and 6%, respectively. The detection rate of the crotonaldehyde-derived DNA adduct $CdG_2$ was 12%. Although crotonaldehyde-induced $CdG_1$ and acrolein-induced 6-OH-$AdG_1$ and 6-OH-$AdG_2$ were also monitored, we could not detect those adducts in any sample. The level of each DNA adduct per $10^8$ bases ranged as follows: 8-oxo-dG, 41.6−837 (median 93.2); $CdG_2$, not detected (ND) to 8.98 (median was under the detection limit); 8-OH-AdG, ND to 3.04 (median 1.14); εdA, ND to 259 (median 4.83); BεdC, ND to 1186 (median was under the detection limit); BεdG, ND to 0.99 (median was under the detection limit; BεdA, ND to 254 (median was under the detection limit); BεmedC, ND to 63.8 (median was under the detection limit); HεdC, ND-8204 (median 10.3); HεdG, ND to 377 (median 15.0); and HεdA, ND to 4186 (median 8.63).

**Adduct Levels of HεdC and BεdC in Different Organs.** As shown in Figure 3, DNA adduct levels of HεdC and BεdC range broadly in different organs. HεdC was detected in all tissue samples except for two liver specimens, whereas BεdC was detected in the colon, kidney, liver, lung, spleen, and pancreas. The median level of HεdC in different organs ranged from 6.4 (kidney) to 23 (colon) adducts per $10^8$ bases, whereas the median of BεdC was 1 or 2 orders of magnitude lower. However, an extremely high level of HεdC (more than 100 adducts per $10^8$ bases) was found in one colon, one lung, one pancreas and two spleen DNA samples, all from different individuals. Also, an extremely high level of BεdC was observed in one lung DNA sample, the same one that showed a high HεdC level as described above. The results suggest that 4-ONE- and 4-OHE-related DNA adducts are widely distributed in various tissues.

Figure 4 shows the correlations of BεdC, εdA, and 8-oxodG with HεdC in human tissue autopsy samples. The DNA adduct level of HεdC was strongly correlated to LPO-induced BεdC ($R^2$ = 0.94) and εdA ($R^2$ = 0.70), but no correlation could be seen between HεdC and the oxidative damage-related lesion 8-oxodG ($R^2$ = 0.02).

## Discussion

In this study, we clearly demonstrated that DNA adducts derived from 4-ONE and 4-OHE occur commonly in human tissues. The levels of the 4-ONE-related DNA adducts HεdC, HεdA, and HεdG in human tissue samples were similar to each other (Supporting Information, Figure S-9), and their median values were 2- to 3-fold higher than that of εdA. However, the 4-OHE-related adducts BεdC, BεmedC, BεdA, and BεdG were detected at lower levels and frequencies; in most samples, their

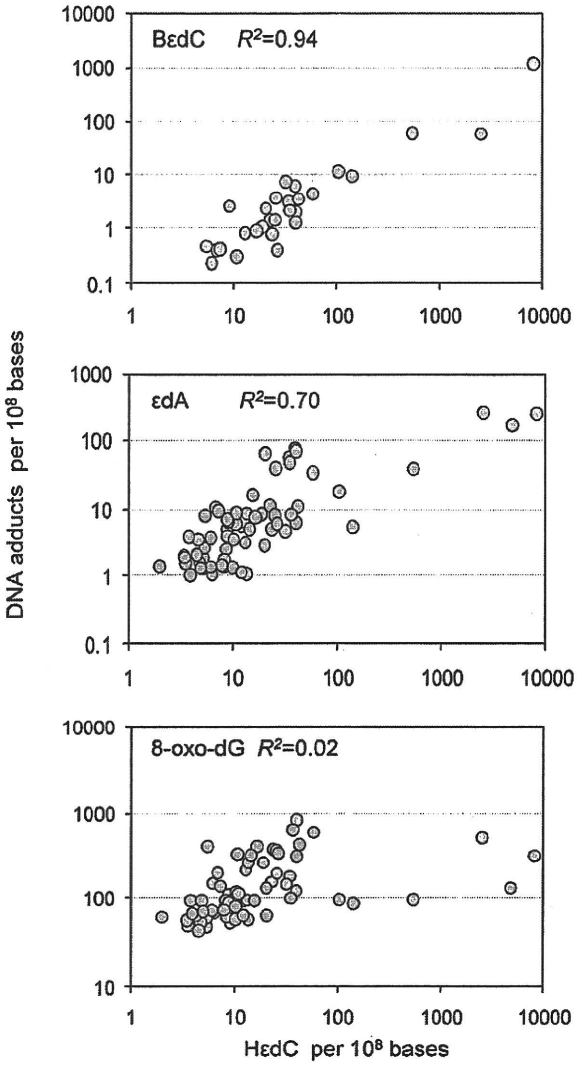


**Figure 4.** Correlations among DNA adduct levels of HεdC vs BεdC, εdA, and 8-oxodG. $R^2$: coefficient of determination. For the $R^2$ calculation, not detected data was treated as 0.

levels were similar to that of crotonaldehyde-derived $CdG_2$ or acrolein-derived 8-OH-AdG. Importantly, in some cases, the levels of these 4-ONE- and 4-OHE-derived DNA adducts were comparable to or even higher than that of the most abundant DNA adduct, 8-oxo-dG. Thus, these recently recognized DNA adducts may be an important source of somatic mutations and could significantly contribute to cancer formation in humans.

The tissues adjacent to those taken for adductome analysis were microscopically examined for the absence of tumor cells. The histological findings varied in terms of inflammation, not otherwise specified. Details of histological characteristics and their relationship to the DNA adducts level are under investigation.

Mutagenic properties of HεdC have been demonstrated in mammalian cell lines and *Escherichia coli* (*26, 27*). Pollack et al. (*26*) reported that in human cell lines HεdC blocked DNA synthesis and also miscoded markedly during the replication of a shuttle vector site-specifically modified with HεdC. The miscoding frequency was higher than 90%, and dT and dA were preferentially inserted opposite the lesion in human cells. HεdC was also shown to be genotoxic in a similar host-vector system consisting of mouse fibroblasts and a replicating plasmid bearing a site-specific HεdC (*25*). Moreover, the results indicated that the Y family DNA polymerases $\eta$, $\kappa$, and $\iota$ preferentially catalyzed the insertion of dT opposite HεdC, whereas an unidentified DNA polymerase was suggested to catalyze the insertion of dA opposite HεdC (*27*). Information about the potential mutagenic properties of the other 4-ONE- and 4-OHE-derived DNA adducts found in human autopsy tissues is still unavailable; thus, further studies concerning the mutagenicity and DNA repair pathways of these newly identified DNA adducts are necessary.

Human tissues could be exposed to 4-ONE and 4-OHE endogenously and exogenously. The endogenous formation of 4-ONE and 4-OHE is via the oxidation of $\omega$6- and $\omega$3-PUFAs in tissues. Because all bodily tissues contain both $\omega$6- and $\omega$3-PUFAs, 4-ONE and 4-OHE could be produced simultaneously under oxidative stress conditions. The near-perfect correlation between the levels of HεdC and BεdC ($R^2 = 0.94$) shown in Figure 4 strongly suggests that there is endogenous and simultaneous formation of 4-ONE- and 4-OHE-derived DNA adducts. According to the slope of the regression curve, the level of HεdC was about 7 times greater than that of BεdC. This also supports the endogenous-formation hypothesis because in all tissues except the brain, the total concentration of $\omega$6- PUFAs is several times higher than that of $\omega$3-PUFAs (*28, 29*).

However, no correlation was observed between the level of HεdC and the level of the oxidative DNA lesion 8-oxo-dG (Figure 4). This discrepancy may be explained by the contribution of enzymatic formation pathways to 4-ONE. For example, Blair's group demonstrated that overexpression of cyclooxygenase-2 (COX-2) increased the level of 4-ONE-derived DNA adducts in both rat intestinal epithelial cells (*30*) and the small intestine of C57BL/6J $APC^{min}$ mice (*31*). COX-2 is an enzyme that is responsible for the formation of the important biological mediator prostaglandin H2. COX-2 can also convert arachidonic acid into 15(*S*)-hydroperoxy-5*Z*,8*Z*,11*Z*,13*E*-eicosatetraenoic acid (15-HPETE), which undergoes homolytic decomposition to the DNA-reactive bifunctional electrophiles 4-hydroperoxy-2(*E*)-nonenal (HPNE), 4,5-epoxy-2(*E*)-decenal (EDE), 4-HNE, and 4-ONE (*31*). 4-ONE is also produced enzymatically from arachidonic acid by the 5-lipoxygenase (5-LO)-related pathway (*32*). 5-LO is an enzyme that is responsible for the formation of leukotriene $A_4$. The precursor of leukotriene $A_4$, 5(*S*)-hydroperoxy-6*E*,8*Z*,11*Z*,14*Z*-eicosatetraenoic acid (5(*S*)-HPETE), generated from arachidonic acid by 5-LO, decomposes to form 4-ONE and HPNE (*32*). The considerably good correlation between the DNA adduct levels of HεdC and εdA, as described in Figure 4 ($R^2 = 0.70$), also suggests the involvement of this metabolic pathway, because εdA is known to be produced by HPNE and EDE (*31*). If 4-OHE is also produced enzymatically from abundant $\omega$3-PUFAs such as docosahexaenoic acid, this would help to explain why the level of BεdC nearly perfectly correlates with the level of HεdC but the level of 8-oxo-dG does not. Further study is needed to elucidate this point.

The exogenous sources of 4-ONE and 4-OHE are foods and cooking vapor. Kasai and Kawai reported that several types of cooked fishes and cooking oils contain 4-OHE in the range of a few to tens of micrograms per gram (*21*). They further reported that the cooking vapor emitted during fish broiling also contains 4-OHE (*21*). In an animal experiment, orally administered 4-OHE resulted in the formation of BεdC, BεdG, and BεmedC in cells of the gastrointestinal tract, but no increase in the level of DNA adducts was observed in the liver and kidney (*19*), indicating that, except for the gastrointestinal tract, the oral route is probably not a significant source of 4-OHE. However, the

impact of cooking vapor in terms of the formation of DNA adducts in pulmonary tissues remains to be resolved.

In conclusion, DNA adducts caused by 4-ONE and 4-OHE are ubiquitous in various human tissues, and even predominant in some cases. It is very likely that these DNA adducts cause somatic mutations and cancers, contribute to aging, and have other adverse effects related to DNA damage. Further studies of their exposure routes and biological properties should be carried out to elucidate the impact of these DNA lesions on human health.

**Acknowledgment.** We thank H. Igarashi and T. Kamo of Hamamatsu University School of Medicine for assistance in collecting the samples. This work was supported by KAKENHI (20014007, 18181883 and 18014009); Grants-in-aid for cancer research from MHLW, Japan; the National Science Council, Taiwan (NSC 98-2221-E-006-020-MY3); NEDO, Japan; and the Smoking Research Foundation.

**Supporting Information Available:** Properties of the patients; sensitivity of LC/MS/MS analysis for each DNA adduct (1 and 2); calibration curves of each DNA adduct; representative chromatographs of DNA adducts, 4-OHE-derived DNA adducts, and 4-ONE-derived DNA adducts in human spleen DNA; DNA adducts level in human tissues; and correlations among the 4-ONE-derived DNA adduct level of HεdC vs HεdA (A) and HεdG (B). This material is available free of charge via the Internet at http://pubs.acs.org.

## References

(1) Cajelli, E., Ferraris, A., and Brambilla, G. (1987) Mutagenicity of 4-hydroxynonenal in V79 Chinese hamster cells. *Mutat. Res. 190*, 169–171.

(2) Nath, R. G., Ocando, J. E., and Chung, F. L. (1996) Detection of 1, N2-propanodeoxyguanosine adducts as potential endogenous DNA lesions in rodent and human tissues. *Cancer Res. 56*, 452–456.

(3) Guillen, M. D., and Goicoechea, E. (2008) Toxic oxygenated alpha-,beta-unsaturated aldehydes and their study in foods: a review. *Crit. Rev. Food Sci. Nutr. 48*, 119–136.

(4) Blair, I. A. (2008) DNA adducts with lipid peroxidation products. *J. Biol. Chem. 283*, 15545–15549.

(5) Markesbery, W. R., and Carney, J. M. (1999) Oxidative alterations in Alzheimer's disease. *Brain Pathol. 9*, 133–146.

(6) Williams, M. V., Wishnok, J. S., and Tannenbaum, S. R. (2007) Covalent adducts arising from the decomposition products of lipid hydroperoxides in the presence of cytochrome c. *Chem. Res. Toxicol. 20*, 767–775.

(7) De Bont, R., and van Larebeke, N. (2004) Endogenous DNA damage in humans: a review of quantitative data. *Mutagenesis 19*, 169–185.

(8) Nair, J., De Flora, S., Izzotti, A., and Bartsch, H. (2007) Lipid peroxidation-derived etheno-DNA adducts in human atherosclerotic lesions. *Mutat. Res. 621*, 95–105.

(9) Wang, H. T., Zhang, S., Hu, Y., and Tang, M. S. (2009) Mutagenicity and Sequence Specificity of Acrolein-DNA Adducts. *Chem. Res. Toxicol. 22*, 511–517.

(10) Uchida, K. (2003) 4-Hydroxy-2-nonenal: a product and mediator of oxidative stress. *Prog. Lipid Res. 42*, 318–343.

(11) Schaur, R. J. (2003) Basic aspects of the biochemical reactivity of 4-hydroxynonenal. *Mol. Aspects Med. 24*, 149–159.

(12) Feng, Z., Hu, W., and Tang, M. S. (2004) Trans-4-hydroxy-2-nonenal inhibits nucleotide excision repair in human cells: a possible mechanism for lipid peroxidation-induced carcinogenesis. *Proc. Natl. Acad. Sci. U.S.A. 101*, 8598–8602.

(13) McGrath, L. T., McGleenon, B. M., Brennan, S., McColl, D., Mc, I. S., and Passmore, A. P. (2001) Increased oxidative stress in Alzheimer's disease as assessed with 4-hydroxynonenal but not malondialdehyde. *Q. J. Med. 94*, 485–490.

(14) Feng, Z., Hu, W., Amin, S., and Tang, M. S. (2003) Mutational spectrum and genotoxicity of the major lipid peroxidation product, trans-4-hydroxy-2-nonenal, induced DNA adducts in nucleotide excision repair-proficient and -deficient human cells. *Biochemistry 42*, 7848–7854.

(15) Zarkovic, N. (2003) 4-hydroxynonenal as a bioactive marker of pathophysiological processes. *Mol. Aspects Med. 24*, 281–291.

(16) Rindgen, D., Nakajima, M., Wehrli, S., Xu, K., and Blair, I. A. (1999) Covalent modifications to 2′-deoxyguanosine by 4-oxo-2-nonenal, a novel product of lipid peroxidation. *Chem. Res. Toxicol. 12*, 1195–1204.

(17) Rindgen, D., Lee, S. H., Nakajima, M., and Blair, I. A. (2000) Formation of a substituted 1, N(6)-etheno-2′-deoxyadenosine adduct by lipid hydroperoxide-mediated generation of 4-oxo-2-nonenal. *Chem. Res. Toxicol. 13*, 846–852.

(18) Pollack, M., Oe, T., Lee, S. H., Silva Elipe, M. V., Arison, B. H., and Blair, I. A. (2003) Characterization of 2′-deoxycytidine adducts derived from 4-oxo-2-nonenal, a novel lipid peroxidation product. *Chem. Res. Toxicol. 16*, 893–900.

(19) Kasai, H., Maekawa, M., Kawai, K., Hachisuka, K., Takahashi, Y., Nakamura, H., Sawa, R., Matsui, S., and Matsuda, T. (2005) 4-oxo-2-hexenal, a mutagen formed by omega-3 fat peroxidation, causes DNA adduct formation in mouse organs. *Ind. Health 43*, 699–701.

(20) Maekawa, M., Kawai, K., Takahashi, Y., Nakamura, H., Watanabe, T., Sawa, R., Hachisuka, K., and Kasai, H. (2006) Identification of 4-oxo-2-hexenal and other direct mutagens formed in model lipid peroxidation reactions as dGuo adducts. *Chem. Res. Toxicol. 19*, 130–138.

(21) Kasai, H., and Kawai, K. (2008) 4-oxo-2-hexenal, a mutagen formed by omega-3 fat peroxidation: occurrence, detection and adduct formation. *Mutat. Res. 659*, 56–59.

(22) Kawai, K., Chou, P. H., Matsuda, T., Inoue, M., Aaltonen, K., Savela, K., Takahashi, Y., Nakamura, H., Kimura, T., Watanabe, T., Sawa, R., Dobashi, K., Li, T. S., and Kasai, H. (2010) DNA modifications by the ω-3 lipid peroxidation-derived mutagen 4-oxo-2-hexenal in vitro and their analysis in mouse and human DNA. *Chem. Res. Toxicol. 23*, 630–636.

(23) Kanaly, R. A., Hanaoka, T., Sugimura, H., Toda, H., Matsui, S., and Matsuda, T. (2006) Development of the adductome approach to detect DNA damage in humans. *Antioxid. Redox Signaling 8*, 993–1001.

(24) Kanaly, R. A., Matsui, S., Hanaoka, T., and Matsuda, T. (2007) Application of the adductome approach to assess intertissue DNA damage variations in human lung and esophagus. *Mutat. Res. 625*, 83–93.

(25) Matsuda, T., Yabushita, H., Kanaly, R. A., Shibutani, S., and Yokoyama, A. (2006) Increased DNA damage in ALDH2-deficient alcoholics. *Chem. Res. Toxicol. 19*, 1374–1378.

(26) Pollack, M., Yang, I. Y., Kim, H. Y., Blair, I. A., and Moriya, M. (2006) Translesion DNA Synthesis across the heptanone−etheno-2′-deoxycytidine adduct in cells. *Chem. Res. Toxicol. 19*, 1074–1079.

(27) Yang, I. Y., Hashimoto, K., de Wind, N., Blair, I. A., and Moriya, M. (2009) Two distinct translesion synthesis pathways across a lipid peroxidation-derived DNA adduct in mammalian cells. *J. Biol. Chem. 284*, 191–198.

(28) Tahin, Q. S., Blum, M., and Carafoli, E. (1981) The fatty acid composition of subcellular membranes of rat liver, heart, and brain: diet-induced modifications. *Eur. J. Biochem. 121*, 5–13.

(29) Engler, M. M., Engler, M. B., Kroetz, D. L., Boswell, K. D. B., Neeley, E., and Krassner, S. M. (1999) The effects of a diet rich in docosahexaenoic acid on organ and vascular fatty acid composition in spontaneously hypertensive rats. *Prostaglandins, Leukotrienes Essent. Fatty Acids 61*, 289–295.

(30) Lee, S. H., Williams, M. V., Dubois, R. N., and Blair, I. A. (2005) Cyclooxygenase-2-mediated DNA damage. *J. Biol. Chem. 280*, 28337–28346.

(31) Williams, M. V., Lee, S. H., Pollack, M., and Blair, I. A. (2006) Endogenous lipid hydroperoxide-mediated DNA-adduct formation in min mice. *J. Biol. Chem. 281*, 10127–10133.

(32) Jian, W., Lee, S. H., Williams, M. V., and Blair, I. A. (2009) 5-Lipoxygenase-mediated endogenous DNA damage. *J. Biol. Chem. 284*, 16799–16807.

TX100047D

OPEN ACCESS Freely available online

PLoS one

# Circadian Disruption Accelerates Tumor Growth and Angio/Stromagenesis through a Wnt Signaling Pathway

**Yoshihiro Yasuniwa[1,2], Hiroto Izumi[1], Ke-Yong Wang[3], Shohei Shimajiri[3], Yasuyuki Sasaguri[3], Kazuaki Kawai[4], Hiroshi Kasai[4], Takashi Shimada[5], Koichi Miyake[5], Eiji Kashiwagi[1], Gen Hirano[1], Akihiko Kidani[1], Masaki Akiyama[1], Bin Han[1,6], Ying Wu[1,7], Ichiro Ieiri[2], Shun Higuchi[7], Kimitoshi Kohno[1]***

1 Department of Molecular Biology, School of Medicine, University of Occupational and Environmental Health, Kitakyushu, Japan, 2 Department of Clinical Pharmacokinetics, Graduate School of Pharmaceutical Sciences, Kyushu University, Fukuoka, Japan, 3 Department of Pathology and Cell Biology, School of Medicine, University of Occupational and Environmental Health, Kitakyushu, Japan, 4 Department of Environmental Oncology, Institute of Industrial Ecological Science, University of Occupational and Environmental Health, Kitakyushu, Japan, 5 Department of Biochemistry and Molecular Biology, Nihon Medical School, Tokyo, Japan, 6 Department of Urology, Shengjing Hospital, China Medical University, Shenyang, China, 7 Department of Oncology, First Affiliated Hospital, China Medical University, Shenyang, China

## Abstract

Epidemiologic studies show a high incidence of cancer in shift workers, suggesting a possible relationship between circadian rhythms and tumorigenesis. However, the precise molecular mechanism played by circadian rhythms in tumor progression is not known. To identify the possible mechanisms underlying tumor progression related to circadian rhythms, we set up nude mouse xenograft models. HeLa cells were injected in nude mice and nude mice were moved to two different cases, one case is exposed to a 24-hour light cycle (L/L), the other is a more "normal" 12-hour light/dark cycle (L/D). We found a significant increase in tumor volume in the L/L group compared with the L/D group. In addition, tumor microvessels and stroma were strongly increased in L/L mice. Although there was a hypervascularization in L/L tumors, there was no associated increase in the production of vascular endothelial cell growth factor (VEGF). DNA microarray analysis showed enhanced expression of WNT10A, and our subsequent study revealed that WNT10A stimulates the growth of both microvascular endothelial cells and fibroblasts in tumors from light-stressed mice, along with marked increases in angio/stromagenesis. Only the tumor stroma stained positive for WNT10A and WNT10A is also highly expressed in keloid dermal fibroblasts but not in normal dermal fibroblasts indicated that WNT10A may be a novel angio/stromagenic growth factor. These findings suggest that circadian disruption induces the progression of malignant tumors via a Wnt signaling pathway.

**Citation:** Yasuniwa Y, Izumi H, Wang K-Y, Shimajiri S, Sasaguri Y, et al. (2010) Circadian Disruption Accelerates Tumor Growth and Angio/Stromagenesis through a Wnt Signaling Pathway. PLoS ONE 5(12): e15330. doi:10.1371/journal.pone.0015330

**Editor:** Sean Bong Lee, National Institute of Diabetes and Digestive and Kidney Diseases/National Institutes of Health, United States of America

**Received** September 12, 2010; **Accepted** November 8, 2010; **Published** December 23, 2010



**Funding:** This work was supported by KAKENHI (17016075), UOEH Grants for Advanced Research and the Vehicle Racing Commemorative Foundation (to K. Kohno). The funders had no role in study design, data collection and analysis, decision to publish, or preparation of the manuscript.

**Competing Interests:** The authors have declared that no competing interests exist.

* E-mail: k-kohno@med.uoeh-u.ac.jp

## Introduction

Modern lifestyles and the use of indoor lighting mean that many people are exposed to a long photoperiod throughout the year [1]. This is most evident in shift workers, especially night workers. This results in the disruption of circadian rhythms, which is known to induce many different types of stress [2]. Abnormal circadian rhythms, including exposure to light at night, are associated with a higher cancer risk and a poorer prognosis [3–7], which may be one of the reasons that the incidence of cancer is increasing in individuals subjected to these stresses. Circadian genes have been shown to function as oncogenes or tumor suppressors at both the systemic and cellular levels due to their roles in cell proliferation, cell cycle regulation, apoptosis and DNA damage signaling pathways [8,9]. However, the molecular or systemic mechanisms involved in tumor growth under artificial illumination stress conditions have not been identified. In fact, the question of whether artificial illumination stress promotes tumor growth at all is still controversial [10,11]. To identify the possible mechanisms underlying tumor progression related to circadian rhythms, we set up nude mouse xenograft models and revealed that artificial light stress induced tumor growth and angio/stromagenesis through WNT10A overexpression.

## Results

### Circadian disruption induces tumor growth and angio/stromagenesis

The mice were divided into two groups: one group was exposed to 24-hour periods of artificial light (L/L) the other was exposed to a more conventional 12-hour light/dark cycle (L/D). First, we examined the effect of light stress on the *in vivo* growth of epidermoid cancer (HeLa) cell tumors and found a significant increase in tumor volume in the L/L group compared with the L/D group (Figure 1A). Similar results were obtained using a xenograft model incorporating prostate cancer (PC3) cells (Figures 1B). Examples of the Hela cell tumors in the L/L and L/D groups are shown in Figure 1C and Figure S1. The L/L tumors were not only larger, but also immunohistochemical analysis showed them to be highly vascular, with increased numbers of CD34 positive ($CD34^+$) and a-Smooth Muscle Actin (a-SMA) positive ($a\text{-}SMA^+$) cells (Figure 1D). High vascularity of

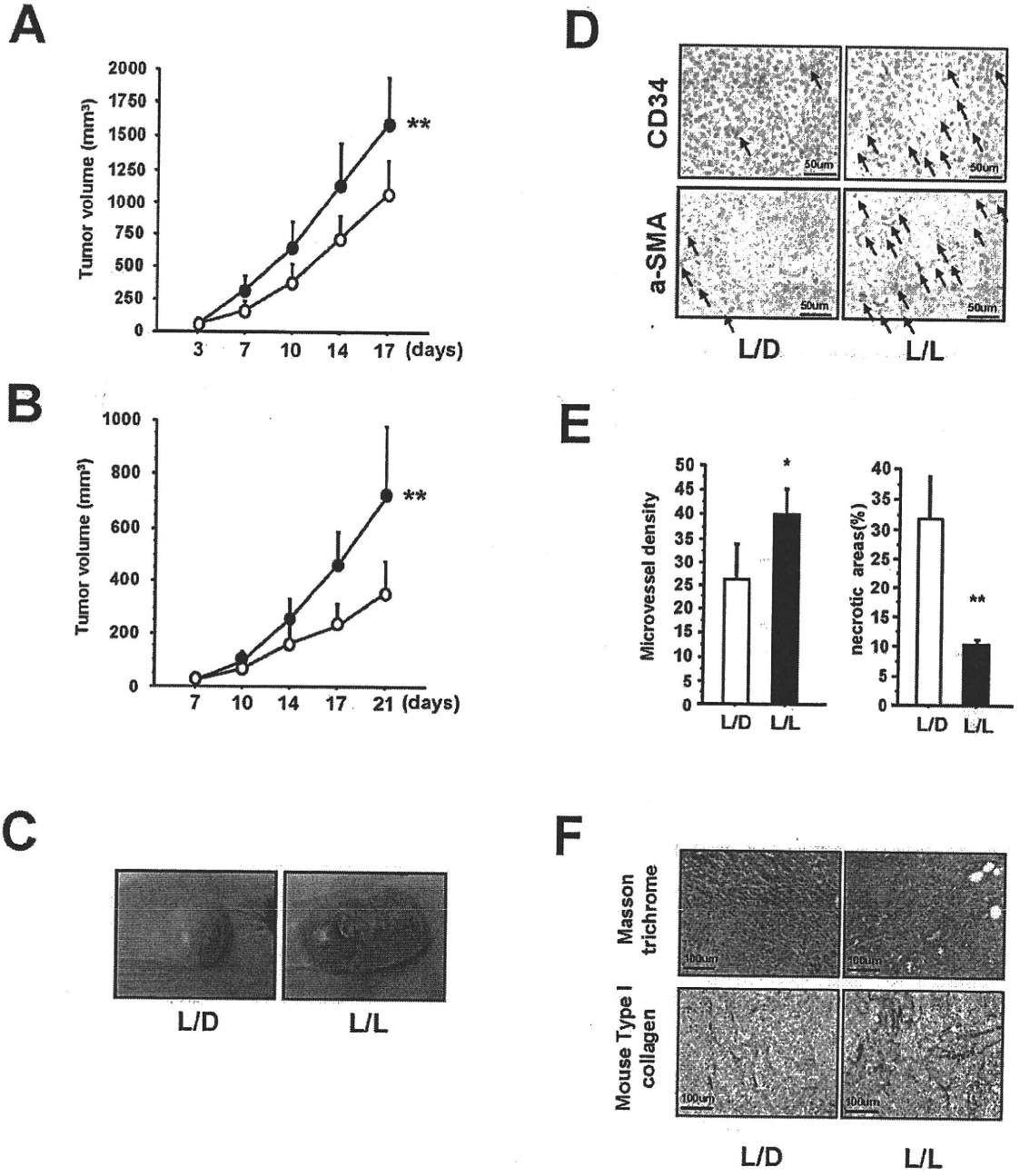


**Figure 1. Effect of photoperiod manipulation on the growth of human HeLa cell or PC3 cell tumors.** (A) Hela cell tumors. Volume of the subcutaneous xenografts in nude mice housed in either L/L (closed circle; $n=16$) or L/D (open circle; $n=16$) conditions. After 17 days of growth, L/L tumors were significantly larger than L/D tumors ($F$ from repeated measure ANOVA = 12.276, $^{**}P<0.01$). (B) PC3 cell tumors. Volume of the subcutaneous xenografts in nude mice housed in either L/L ($n=8$) or L/D ($n=8$) conditions. A significant reduction in volume is seen in the L/D tumors compared with the L/L tumors ($F$ from repeated measure ANOVA = 18.360, $^{**}P<0.01$). (C) Representative photograph of L/L and L/D tumors showing the obvious difference in size. (D) Immunohistochemical analysis of CD34 positive ($CD34^+$) cells and aSMA positive ($aSMA^+$) cells in the L/L and L/D tumors. Increased numbers of $CD34^+$ and $aSMA^+$ (black arrows) are clearly visible in the L/L tumors. (E) The number of microvessels was quantified using the number of $CD34^+$ cells. An increase in microvessel density (vessels in 10 viewing fields; $n=3$ per group, $^{*}P<0.05$), is accompanied by a decrease in necrosis ($n=3$ per group $^{**}P<0.01$). (F) Representative photographs showing masson trichrome staining of the expanded extracellular matrix and immunohistochemical analysis of mouse Type I collagen in the L/D and L/L tumors.
doi:10.1371/journal.pone.0015330.g001

tumor surface in L/L group using HeLa cells was reproducibly observed in four independent experiments. Also, the microvessel density within the L/L tumors was significantly higher than that in the L/D tumors and correlated with a reduction in the amount of necrosis (Figure 1E). Masson trichrome staining of the tumor stroma showed a clear expansion of the extracellular matrix

(ECM; stained blue) in the L/L tumors not seen in the L/D tumors (Figure 1F). The immunostaining of mouse Type I collagen also showed the increase of ECM in the L/L tumors (Figure 1F). Taken together, these results clearly show that abnormal circadian rhythms induce marked tumor growth accompanied by increased angio/stromagenesis.

## Microarray analysis of L/L tumors and L/D tumors

Next, we wanted to investigate the molecular mechanisms underlying the striking morphological differences between L/L and L/D tumors. Whole-genome expression DNA microarray analysis was performed to identify the genes and biological pathways that might be regulated by photoperiod manipulation. We found that 201 genes were transcriptionally upregulated in the L/L tumors compared with the L/D tumors (Table S1). Surprisingly, the expression of human VEGF-A and VEGF-B, which are the most important molecules in cancer angiogenesis, was the same in L/L and L/D tumors (Table S1 and Figure 2A), suggesting that a novel angiogenic factor is involved in increased L/L tumor growth. We focused on genes encoding secretory proteins (Table 1) and found a greater than 9-fold upregulation in the expression of WNT10A in L/L tumors compared with L/D tumors. We designed human WNT10A and mouse Wnt10a specific primers for semi-quantitative RT-PCR analysis and checked the specificity of the primers (Figures S2A and Table S2). Semi-quantitative RT-PCR showed that not only human WNT10A, but also mouse Wnt10a, was upregulated in L/L tumors (Figure 2A); however, the expression of human WNT10A in the L/L tumors was still very low as it could only be detected using nested techniques (1st PCR 30 cycles and 2nd PCR 35 cycles). Immunohistochemical analysis showed WNT10A expression mainly around the blood vessels and it was increased in L/L tumors compared with L/D tumors (arrows in Figure 2B), indicating that this enhanced expression of WNT10A is derived from mouse tissues.

## WNT10A overexpression cells induce tumor growth, angiogenesis and stromagenesis in vivo xenograft models

To further investigate the role played by WNT10A in these morphological changes, we established another nude mouse model implanted with HeLa cells overexpressing WNT10A (Figures 3A and S3). Because the growth rate of these WNT10A-overexpressing cells was similar to that of control cells *in vitro* (Figure 3B), we were surprised to see that the growth rate of the implanted WNT10A-overexpressing tumors was faster than that of control tumors (Figure 3C). Furthermore, as shown in Figure 3D, most of the tumors were hypervascular; even those from mice housed under L/D conditions. Immunohistochemical analysis of these WNT10A-overexpressing tumors showed increased numbers of a-SMA$^+$ cells coupled with increased size, microvessel density, significantly reduced areas of necrosis (Figures 3E and 3F) and an expanded ECM (Figure 3G).

## WNT10A is expressed in fibroblasts and WNT10A stimulates the growth of both fibroblasts and vascular endothelial cells in vitro

Based on these results, we hypothesized that WNT10A was functioning as a growth factor for both vascular endothelial cells and fibroblasts and was involved in a novel mechanism of tumor growth, possibly via the promotion of angio/stromagenesis. To confirm this hypothesis, we used RT-PCR to show that normal human dermal fibroblasts (NHDF) cells express WNT10A, but

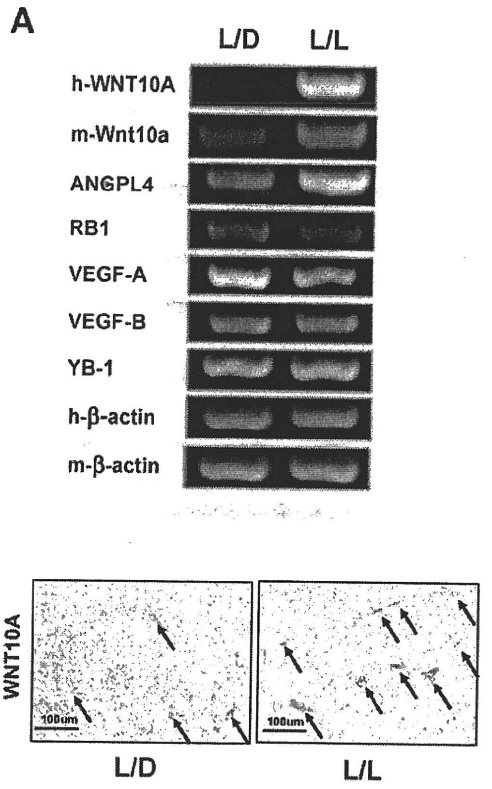


**Figure 2. WNT10A was upregulated in L/L tumors.** (A) RT-PCR of the relevant gene transcripts was carried out based on the results of the DNA microarray analysis. Human WNT10A (h-WNT10), mouse Wnt10a (m-Wnt10a) and ANGPL4 were upregulated in L/L mice tumors. RB1 was downregulated. There was no difference in the expression levels of VEGF-A, VEGF-B and YB-1 between L/L and L/D tumors. Human β-actin (h-β-actin) and mouse β-actin (m-β-actin) were used as internal control. The cycle number is 30 for all semi-quantitative RT-PCR except h-WNT10A. Nested PCR technique to investigate the expression of human WNT10A in tumors. The cycle number of 1st PCR is 30 and that of 2nd nested PCR is 35. (B) Immunohistochemical analysis of WNT10A in L/L and L/D mice tumors. The arrows indicate tumor blood vessels.
doi:10.1371/journal.pone.0015330.g002

normal human dermal microvascular endothelial (HMVEC-d) cells do not (Figure 4A). This suggests the presence of a WNT10A-dependent autocrine growth system in fibroblasts. Cell proliferation analysis showed that the growth of both HMVEC-d and NHDF cells was stimulated by the addition of conditioned medium from WNT10A-overexpressing cells and was significantly inhibited by the addition of an anti-WNT10 antibody (Figures 4B and 4C). NHDF cells cultured in recommended medium were also effectively inhibited by the addition of the anti-WNT10A antibody (Figure 4D). In addition, knockdown of WNT10A-expression using siRNA inhibited the growth of NHDF cells (Figures 4E and 4F), confirming the existence of a WNT10A-dependent autocrine growth mechanism.

## Tumor stroma cells express WNT10A

The pattern of WNT10A expression in human tumors was examined by immunohistochemistry (Figures 5A and 5B). A careful examination of the double stained tissues showed marked increase of WNT10A positive fibroblastic cells in scirrhous type gastric cancer which is a representative cancer with hyperplastic

**Table 1.** The subset of secretory protein genes was selected if fold change marked more than 2.0 in the L/L tumor sample compared to the L/D tumor sample.

| Gene symbol | Accession number | Fold change | Gene discription |
|---|---|---|---|
| WNT10A | NM_025216 | 9.41 | Protein WNT-10A precursor. |
| CCL11 | NM_002986 | 3.06 | Eotaxin precursor (Small inducible cytokine A11). |
| MUC1 | NM_002456 | 2.79 | Mucin-1 precursor. |
| SCGB1C1 | NM_145651 | 2.51 | Secretoglobin family 1C member 1 precursor. |
| ANGPTL4 | NM_016109 | 2.36 | Angiopoietin-related protein 4 precursor (Angiopoietin-like 4). |
| CES1 | NM_001266 | 2.30 | Liver carboxylesterase 1 precursor. |
| EDN1 | NM_001955 | 2.20 | Endothelin-1 precursor. |
| AMY2A | NM_000699 | 2.19 | Pancreatic alpha-amylase precursor. |
| C1QTNF6 | NM_031910 | 2.13 | Complement C1q tumor necrosis factor-related protein 6 precursor. |
| HTRA3 | NM_053044 | 2.08 | Probable serine protease HTRA3 precursor. |
| FBLN1 | NM_006486 | 2.04 | Fibulin-1 precursor. |
| APOC1 | NM_001645 | 2.03 | Apolipoprotein C-I precursor. |

doi:10.1371/journal.pone.0015330.t001

stroma (Figure 5A). Only the tumor stroma stained positive for WNT10A, strongly suggesting expression by stromal cells such as fibroblasts, myofibroblasts, smooth muscle cells, and pericytes.

### WNT10A is expressed in keloid stroma, but not in normal dermal stroma

The inducible expression of Wnt genes, including WNT10A, stimulates the proliferation of hepatic progenitor cells [12], and mutations in WNT10A are associated with an autosomal recessive ectodermal dysplasia [13,14]. In addition, The expression of Wnt signaling antagonists has been shown to be down-regulated in keloid, which is an aggressive wound healing tissue, fibroblasts [15,16]. These previous reports indicate that WNT signaling is involved in both tissue repair and wound healing. Because an old hypothesis suggests that cancer results from uncontrolled wound-healing [17], we investigated WNT10A expression in keloid tissue. WNT10A-positive cells were only found in the vessels and peripheral nerves of normal skin (Figure 6A). On the other hand, WNT10A expression markedly increased in fibroblastic cells in the hyperplastic stroma of keloid tissue (Figure 6B), suggesting that WNT10A functions as an angio/stromagenesis gene in tumor progression, thus supporting the "old" hypothesis. Although WNT10A expression was observed in cutured normal human dermal fibroblasts (Figure 4E), WNT10A expression was not in fibroblast in normal skin (Figure 6A). This may be probably due to the sensitivity of immunostaining analysis. Another possibility is that normal human dermal fibroblasts were cultured with growth factors which may induce the WNT10A expression.

### Oxidative stress induce WNT10A expression

The level of psychological and physiological stress experienced by the mice is hard to measure experimentally. So, we measured 8-OH deoxyguanosine (8-OH-dG) associated with increased levels of oxidative stress. We found that the level of 8-OH-dG in lung tissue, but not liver, from L/L mice was significantly higher than that in L/D mice (Figure 7A). This is consistent with the fact that lung tissue is more sensitive to oxidative DNA damage than other tissues [18]. This data strongly suggest an association between disruption of circadian rhythms and increased oxidative stress responses. A preliminary study also showed that the promoter activity of the WNT10A gene was induced by the oxidizing agent, hydrogen peroxide and Wnt10a mRNA transcript level was also increased in NIH3T3 cells treated with hydrogen peroxide (Figures 7B and 7C). These provide further evidence supporting the role of oxidative stress in tumor promotion and progression.

## Discussion

Greater understanding of the complexity of the tumor microenvironment, and the role of tumor angiogenesis, will lead to further advances in cancer treatment [4,19,20]. The results presented in this paper are both interesting and unexpected and strongly suggest that disruption of circadian rhythms promotes tumor growth through WNT10A-dependent angio/stromagenesis resulting from increased levels of oxidative stress. The transcriptional factor of NF-κB is activated by oxidative stress or tumor necrosis factor alpha (TNF-α) [21]. WNT10A has been shown to be one of the NF-κB target genes and it's expression was induced by TNF-α [22,23]. Since there is one NF-kB site in the promoter region of WNT10A gene, it is conceivable that WNT10A might be regulated by NF-κB pathway. WNT signaling pathway has been implicated in angiogenesis [24] and tumor stroma microenvironment [25]. These data suggest that both endothelial cells and stromal cells are activated by WNT signals from cancer cells. On the other hand, our data indicate that both endothelial cells and stromal cells may be activated by WNT10A signals from non tumor cells, such as cancer associated fibroblasts. WNT signaling has been separated into a "canonical" pathway or "non-canonical" pathways [26]. Since canonical WNT signaling pathway stabilize β-catenin, we hypothesized that WNT10A might also stabilize β-catenin. The expression of β-catenin was observed in the endothelial cells of newly formed tumor vessels (Figure S4), suggesting that Wnt/β-catenin signaling plays a role in tumor angiogenesis. WNT signaling is also known to play an important role in cancer and stem cell biology [27], indicating that WNT10A might affect not only the tumor microenvironment, but also stem cells themselves.

There are some limitations in this study. We cannot exclude the possibility that other physiological and/or hormonal factors, such as melatonin, affected the growth of the implanted cancer cells in our mouse models [28–30]. Subcutaneous injection of rapidly growing human cancer cells into nude mice provided a setting in which tumor growth could be assessed in a relatively short time

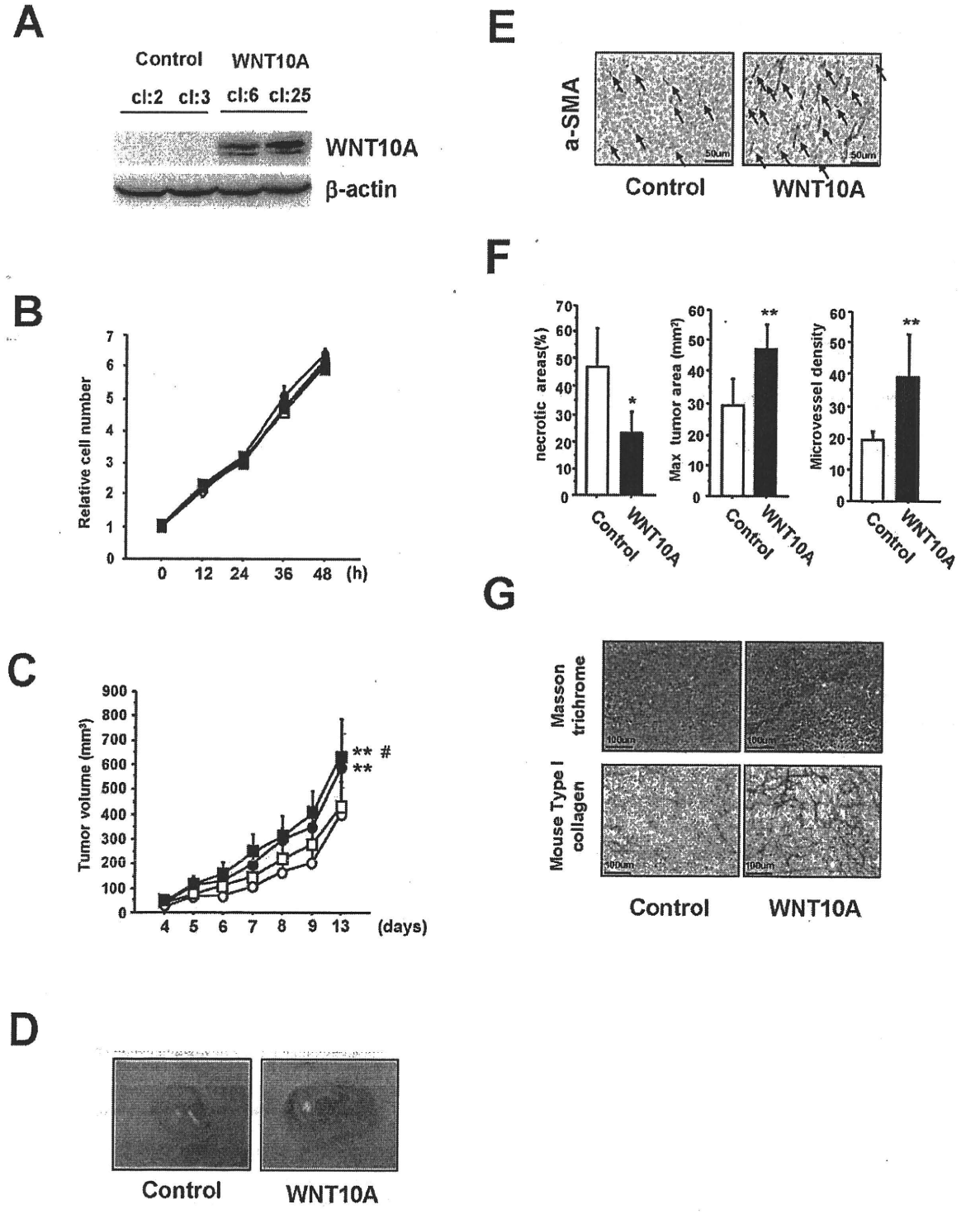


**Figure 3. WNT10A functions as an angio/stromagenetic growth factor *in vivo* xenograft models.** (A) Establishment of á stable WNT10A-overexpressing cell line. (B), (C) The growth rate of these stable cell lines (B) *in vitro* and (C) *in vivo*. Two control cell lines (cl:2; open circle, cl:3; open square) and two stable WNT10A-overexpressing cell lines (cl:6; closed circle, cl:25, closed square) were used. $^{**}P<0.01$ compared with the control cl:2 group and $\#P<0.05$ compared with the control cl:3 group using Scheffe's test. $n=8$ per groups. (D) Representative photograph WNT10A-overexpressing tumors in nude mice illustrating their hypervascular nature. (E) Immunostaining of tumors with an anti-aSMA antibody. Increased numbers of $aSMA^+$ cells (black arrows) are clearly visible in WNT10A-overexpressing tumors. (F) Reduced areas of tissue necrosis in WNT10A-overexpressing tumors are accompanied by increased tumor size and increased microvessel density ($n=4$ or 6 per group, $^*P<0.05$ and $^{**}P<0.01$). Microvessel density was quantified using the number of $aSMA^+$ cells (G) Masson trichrome staining showing expansion of the extracellular matrix and immunohistchemical analysis of mouse Type I collagen in the control and WNT10A-overexpressing tumors.
doi:10.1371/journal.pone.0015330.g003

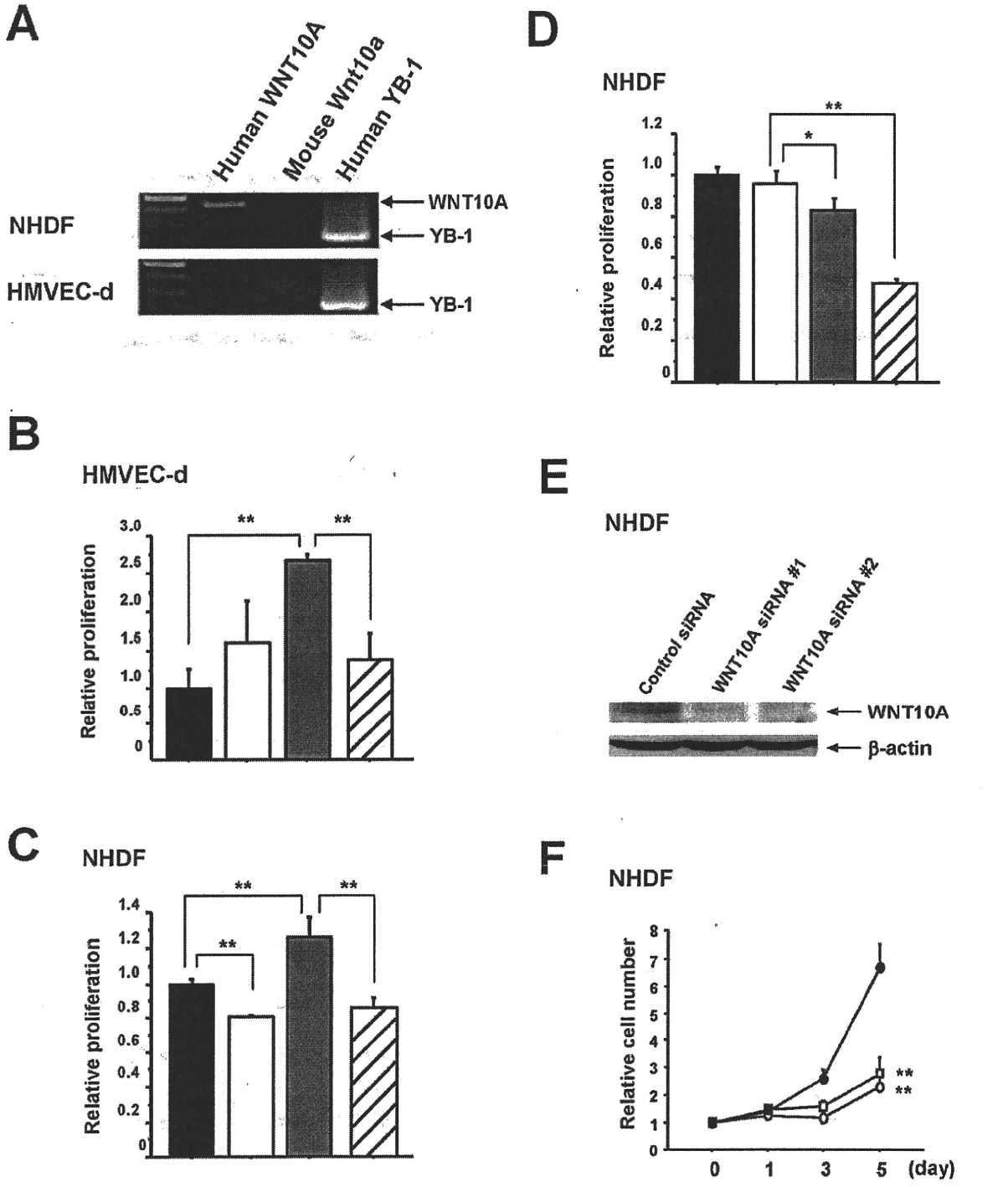


**Figure 4. WNT10A is expressed in fibroblast cells and functions as an angio/stromagenesis growth factor *in vitro*.** (A) RT-PCR for human WNT10A mRNA in NHDF and HMVEC-d cells. Human YB-1 was used as a positive control and mouse Wnt10a was used as a negative control. (B), (C) WNT10A-dependent growth of HMVEC-d and NHDF cells. For the proliferation assays using BrdU incorporation, HMVEC-d (NHDF) cells were cultured in conditioned medium (CM) with or without WNT10A antibody for 24 hours (black bar; Control-CM, white bar; Control-CM + WNT10A antibody 5 μg/ml, gray bar; WNT10A-CM, slash bar; WNT10A-CM + WNT10A antibody 5 μg/ml). $^{**}P<0.01$. $n=3$ per groups. (D) WNT10A-dependent autocrine growth of NHDF cells. NHDF cells were cultured with the recommended medium (RM) with or without WNT10A antibody (black bar; RM, white bar; RM + IgG 5 μg/ml, gray bar; RM + WNT10A antibody 2 μg/ml, slash bar; RM + WNT10A antibody 5 μg/ml). $^{*}P<0.05$ and $^{**}P<0.01$. $n=3$ per groups. (E) Complete knockdown of WNT10A expression in NHDF cells is achieved using the two siRNAs against WNT10A. Whole-cell extracts (100 μg) were subjected to SDS-PAGE, and Western blotting analysis was performed using the indicated antibodies. (F) Knockdown of WNT10A suppresses the growth of NHDF cells (Control siRNA; closed circle, WNT10A siRNA #1; open square, WNT10A siRNA #2; open circle). $^{**}P<0.01$ compared with the control siRNA group.

doi:10.1371/journal.pone.0015330.g004

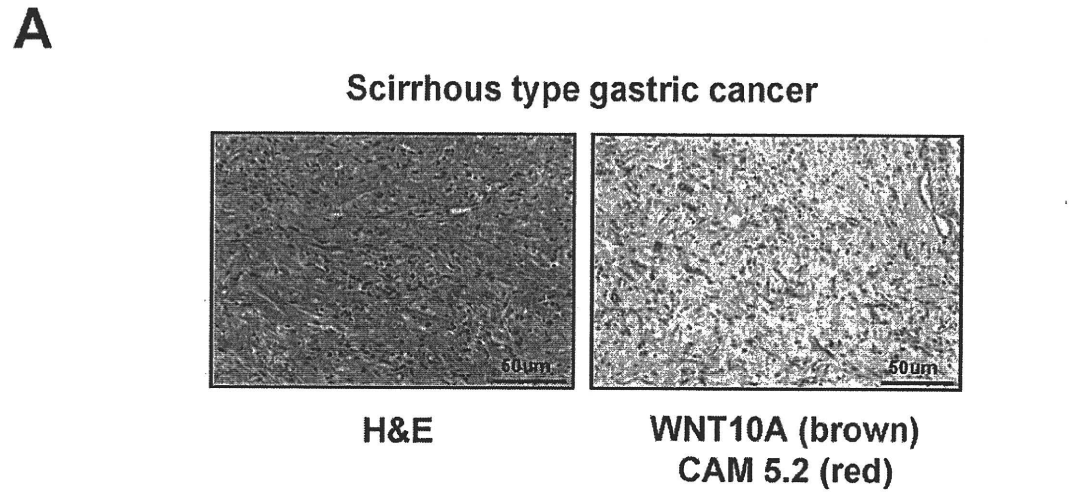


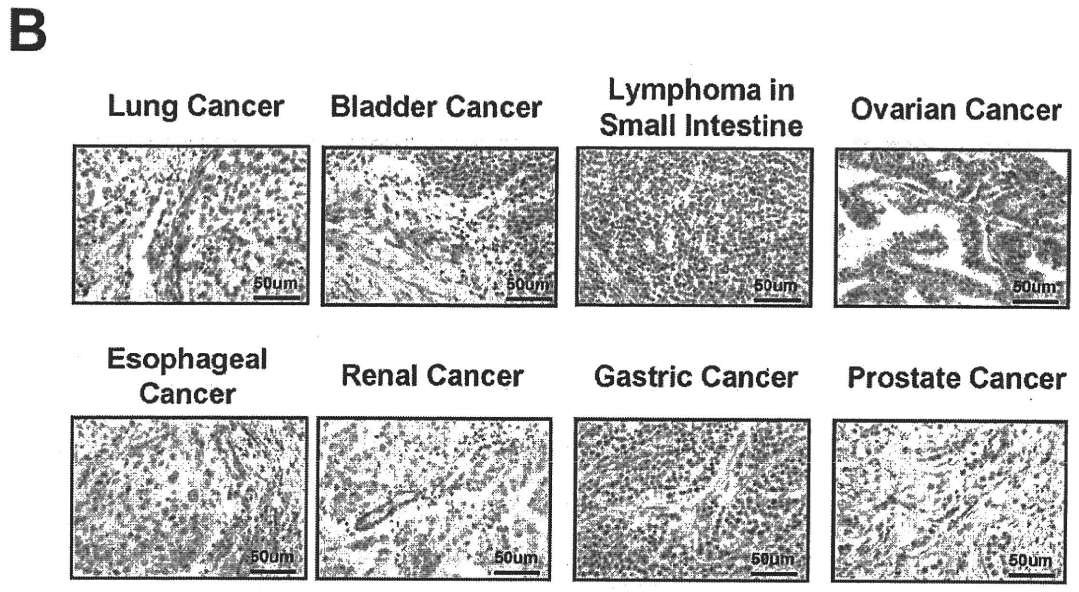


**Figure 5. Immunohistochemical analysis of WNT10A expression in various human cancer specimens.** (A) H&E and double immunohistochemical staining of scirrhous-type signet-ring carcinoma cells. 3,3′-Diaminobenzidine (DAB) was used as chromogen for WNT10A staining (brown color) and Vulcan fast red was used for cytokeratin CAM 5.2 staining (red color). Anti-cytokeratin CAM 5.2 was used for staining of signet-ring cell carcinoma cells. (B) WNT10A expresses cancer stroma cells in various human cancer specimens. 3,3′-Diaminobenzidine (DAB) was used as chromogen for WNT10A staining (brown color).
doi:10.1371/journal.pone.0015330.g005

span. Orthotopic model will be a better way to confirm our results because it more accurately reproduces the interactions between tumor cells and their microenvironment [31]. Nevertheless, our data clearly show that WNT10A has angio/stromagenic activity. Further analysis is required to clarify whether WNT10A-Frizzled binding mediates cell proliferation in both endothelial cells and stromal cells. Examining WNT10A receptors and associated signal transduction pathways may provide valuable insights into the role of circadian rhythms in tumor progression [32,33]. Our findings not only support the emerging links between circadian rhythm, oxidative stress and tumor progression at the molecular level, but also warn of the adverse effects of artificial light.

## Materials and Methods

### Primary cells, cell lines and culture conditions

HMVEC-d and NHDF cells were purchased from Lonza Co. HMVEC-d and NHDF cells were maintained with EGM-2-MV BulletKit and FGM-2 BulletKit (Lonza Co), respectively. HMVEC-d cells were cultured in endothelial cell basic medium (EBM) containing 5% FBS and a growth factor mixture containing hydrocortisone, ascorbic acid, FGF, VEGF, IGF, EGF and gentamycin. NHDF cells were cultured in fibroblast basic medium (FBM) containing 2%, FBS containing the appropriate growth factors (insulin, FGF, and gentamycin). The human prostate cancer

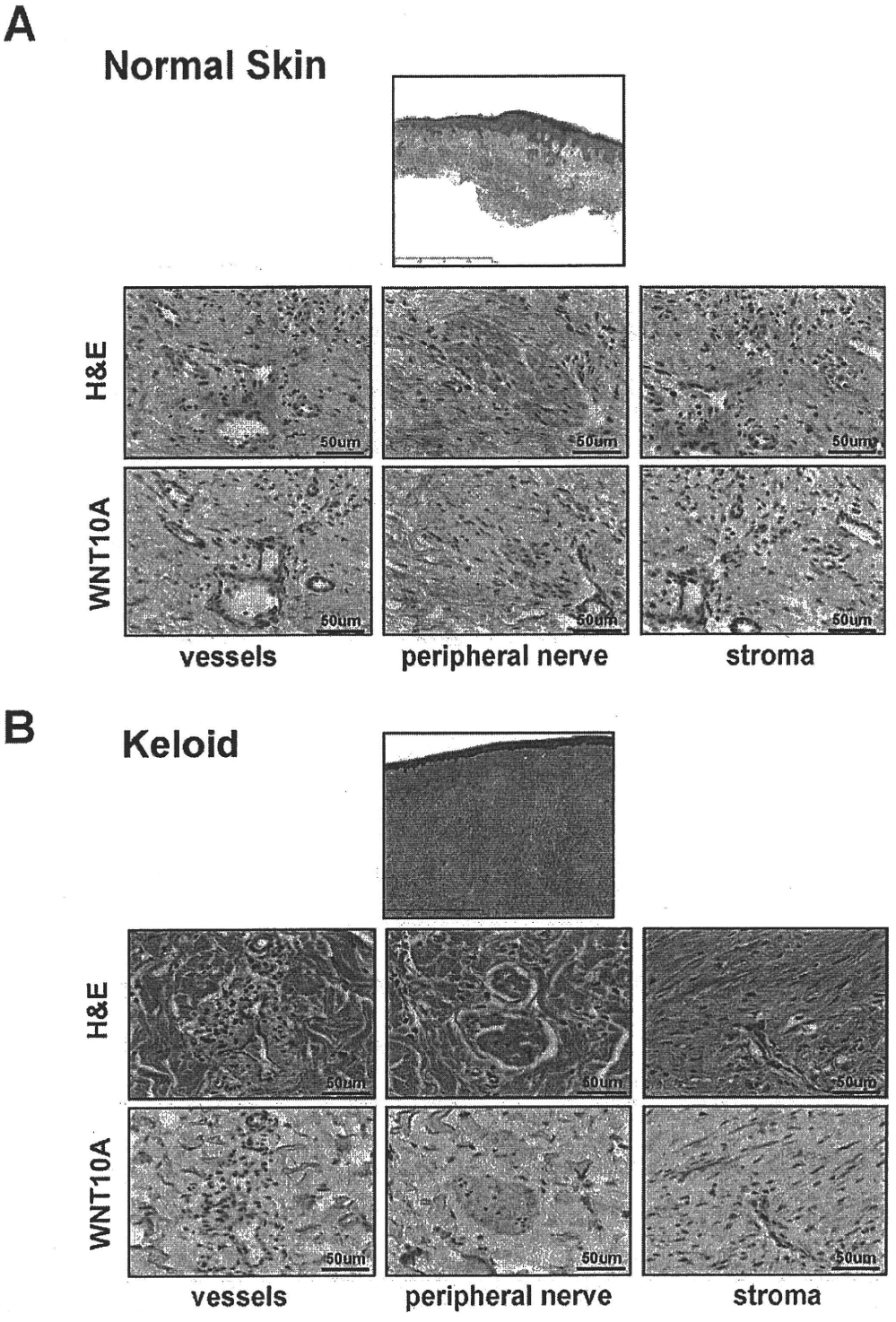


**Figure 6. WNT10A is expressed in stromal cells of keloid tissue.** H&E and anti-WNT10A antibody staining in (A) normal skin and (B) keloid tissue. WNT10A was expressed around the vessels and in the peripheral nerve cells of normal skin, but not in stromal cells. In contrast, WNT10A was expressed around vessels, in peripheral nerve cells and strongly in stromal cells of keloid tissue. Vulcan fast red was used for WNT10A staining (red color).
doi:10.1371/journal.pone.0015330.g006